

## HUBBLE SPACE TELESCOPE NICMOS OBSERVATIONS OF T DWARFS: BROWN DWARF MULTIPLICITY AND NEW PROBES OF THE L/T TRANSITION

ADAM J. BURGASSER<sup>1</sup>, J. DAVY KIRKPATRICK<sup>2</sup>, KELLE L. CRUZ<sup>3,4</sup>, I. NEILL REID<sup>5</sup>, SANDY K. LEGGETT<sup>6</sup>, JAMES LIEBERT<sup>7</sup>,  
ADAM BURROWS<sup>7</sup>, AND MICHAEL E. BROWN<sup>8</sup>

*Submitted to ApJ, 30 March 2006; Accepted, 22 May 2006*

### ABSTRACT

We present the results of a Hubble Space Telescope NICMOS imaging survey of 22 T-type field brown dwarfs. Five are resolved as binary systems with angular separations of  $0''.05$ – $0''.35$ , and companionship is established on the basis of component F110W–F170M colors (indicative of CH<sub>4</sub> absorption) and low probabilities of background contamination. Prior ground-based observations show 2MASS 1553+1532AB to be a common proper motion binary. The properties of these systems – low multiplicity fraction ( $11^{+7}_{-3}\%$  resolved, as corrected for sample selection biases), close projected separations ( $\rho = 1.8$ – $5.0$  AU) and near-unity mass ratios — are consistent with previous results for field brown dwarf binaries. Three of the binaries, 2MASS 0518-2828AB, SDSS 0423-0414AB and SDSS 1021-0304AB, have components that span the poorly-understood transition between L dwarfs and T dwarfs. Spectral decomposition analysis of SDSS 1021-0304AB reveals a peculiar flux reversal in this system, with a T5 secondary that is  $\sim 30\%$  brighter at  $1.05$  and  $1.27 \mu\text{m}$  than the T1 primary. This system, 2MASS 0518-2828AB and SDSS 1534+1615 all demonstrate that the *J*-band brightening observed between late-type L to mid-type T dwarfs is an intrinsic feature of this spectral transition, albeit less pronounced than previously surmised. We also find that the resolved binary fraction of L7 to T3.5 dwarfs is twice that of other L and T dwarfs, an anomaly that can be explained by a relatively rapid evolution of brown dwarfs through the L/T transition, perhaps driven by dynamic (nonequilibrium) depletion of photospheric condensates.

*Subject headings:* stars: binaries: visual — stars: fundamental parameters — stars: individual (SDSS J042348.57–041403.5, 2MASS J05185995–2828372, SDSS J092615.38+584720.9, SDSS J102109.69–030420.1, 2MASS J15530228+1532369) — stars: low mass, brown dwarfs

### 1. INTRODUCTION

Multiple star systems are of fundamental importance in the study of stellar populations, and by inference much of galactic and extragalactic astrophysics. These systems remain the predominant outlet for the direct measurement of individual stellar masses, either through the detection of orbital motion or microlensing techniques (An et al. 2002). Eclipsing binaries also enable measurement of stellar radii. The properties of and interactions between the components of multiple star systems are fundamental to the phenomena of cataclysmic variables, X-ray binaries, Type Ia supernovae, planetary nebulae and several classes of peculiar stars. Indeed, the creation of multiple systems is inherent in the star formation process itself. Measurement of multiplicity statistics — the binary fraction, mass ratio distribution and separation

distribution — provide key empirical constraints on star formation theory. The formation and character of planet-forming debris disks around young stars can be modulated by the presence of companions. Finally, coeval binary systems provide a unique control environment for studying the detailed physical properties of individual stars, yielding insight on the general characteristics of a stellar class.

Multiple systems have been particularly useful in the study of brown dwarfs, stars with insufficient mass to sustain core hydrogen fusion (Kumar 1962; Hayashi & Nakano 1963). Indeed, many of the first brown dwarfs to be identified are members of nearby multiple systems (Becklin & Zuckerman 1988; Nakajima et al. 1995; Oppenheimer et al. 1995; Rebolo et al. 1998). Over the past few years, high resolution imaging and spectroscopic surveys of very low mass (VLM;  $M \lesssim 0.1M_{\odot}$ ) stars and brown dwarfs in the field and in young stellar clusters have revealed roughly 75 binaries (cf. Burgasser et al. 2006b<sup>9</sup>), with intriguing results. The resolved VLM binary fraction (the frequency of binary systems in a given sample of stars) is  $\sim 10$ – $20\%$ , significantly lower than the binary fractions of solar-type stellar systems ( $\sim 65\%$ ; e.g. Abt & Levy 1976; Duquennoy & Mayor 1991) and early-type M stars ( $\sim 30$ – $40\%$ ; e.g. Fischer & Marcy 1992; Reid & Gizis 1997; Delfosse

<sup>1</sup> Massachusetts Institute of Technology, Kavli Institute for Astrophysics and Space Research, Building 37, Room 664B, 77 Massachusetts Avenue, Cambridge, MA 02139; ajb@mit.edu

<sup>2</sup> Infrared Processing and Analysis Center, M/S 100-22, California Institute of Technology, Pasadena, CA 91125

<sup>3</sup> Department of Astrophysics, American Museum of Natural History, Central Park West at 79th Street, New York, NY 10024

<sup>4</sup> NSF Astronomy and Astrophysics Postdoctoral Fellow

<sup>5</sup> Space Telescope Science Institute, 3700 San Martin Drive, Baltimore, MD 21218

<sup>6</sup> Joint Astronomy Centre, 660 North A'ohoku Place, Hilo, HI 96720

<sup>7</sup> Steward Observatory, University of Arizona, 933 North Cherry Avenue, Tucson, AZ 85721

<sup>8</sup> Division of Geological and Planetary Sciences, M/S 105-21, California Institute of Technology, Pasadena, California 91125

<sup>9</sup> A current list of known VLM binaries is maintained by N. Siegler at the Very Low Mass Binaries Archive, [http://paperclip.as.arizona.edu/~sim\\$nsiegler/VLM\\_binaries/](http://paperclip.as.arizona.edu/~sim$nsiegler/VLM_binaries/).

et al. 2004), indicating a decline in the binary fraction with later spectral types (Bouy et al. 2006). The resolved binary fraction is likely a lower limit to the true binary fraction due to the existence of unresolved, closely separated systems (Maxted & Jeffries 2005). This possibility is an important consideration for low-mass systems, for while the distribution of separations of F-through M-type stellar pairs is quite broad, ranging over 0.1 AU to 0.1 pc, >90% of all known VLM binaries have projected separations <20 AU (Burgasser et al. 2006b), with maximum separations scaling with total system mass (Close et al. 2003; Burgasser et al. 2003c, however, see Luhman 2004 and Billeres et al. 2005). The mass ratio distribution of resolved VLM binaries is also distinct, peaking sharply at  $q \equiv M_2/M_1 \approx 1$  (Reid et al. 2001; Bouy et al. 2003; Burgasser et al. 2003c), in contrast to the relatively flat mass ratio distributions of stellar systems (e.g., Mazeh et al. 1992). These properties have led researchers to suggest that VLM stars and brown dwarfs may form via a different mechanism than stars (e.g., Bate, Bonnell & Bromm 2002), although this idea remains controversial (e.g., Luhman 2004). More concretely, astrometric and spectroscopic followup of VLM binaries have provided the first brown dwarf mass measurements (Basri & Martín 1999; Lane et al. 2001; Bouy et al. 2004; Brandner et al. 2004; Zapatero Osorio et al. 2004; Stassun et al. 2006), important empirical constraints for theoretical evolutionary models.

In order to constrain the binary properties of brown dwarfs in greater detail, to identify new systems useful for mass measurements, and to search for very low luminosity brown dwarf companions, we have conducted a high resolution imaging survey of 22 T dwarfs using NICMOS on the *Hubble Space Telescope* (hereafter, *HST*). T dwarfs are the lowest luminosity ( $L \lesssim 3 \times 10^{-5} L_\odot$ ) and coldest ( $T_{eff} \lesssim 1400$  K; Golimowski et al. 2004) brown dwarfs currently known. They are distinguished by the presence of strong H<sub>2</sub>O and CH<sub>4</sub> absorption bands in their near infrared spectra (Burgasser et al. 2002c; Geballe et al. 2002) and the absence of photospheric condensates that dominate warmer L dwarf atmospheres (Marley et al. 1996; Tsuji et al. 1996; Allard et al. 2001). We have identified five binaries in our sample, of which three have well-resolved components allowing detailed characterization of their empirical properties.

Observations are described in § 2, including the sample composition, observing strategy and data reduction. In § 3 we present photometric results, including color/spectral type, photometric conversion and bolometric correction relations. In § 4 we describe point spread function (PSF) fits to our resolved sources, and determine sensitivity limits for putative faint companions. Detailed analysis of individual systems is given in § 5. In § 6 we provide an updated assessment of the multiplicity properties of field brown dwarfs, including the overall binary fraction, separation distribution and mass ratio distribution. In § 7 we examine what currently known brown dwarf binaries reveal about the poorly understood transition between L dwarfs and T dwarfs. Results are summarized in § 8.

## 2. OBSERVATIONS

### 2.1. T Dwarf Targets

Observations presented here incorporate data from two *HST* programs, GO-9833 and GO-10247 conducted during Cycles 12 and 13, respectively. The first program targeted 22 T dwarfs identified in the Sloan Digital Sky Survey (York et al. 2000, hereafter SDSS) and the Two Micron All Sky Survey (Skrutskie et al. 2006, hereafter 2MASS), spanning the full range of T spectral types (T0 to T8), including the lowest luminosity brown dwarf so far identified, 2MASS 0415-0935<sup>10</sup> (Burgasser et al. 2002c; Vrba et al. 2004; Golimowski et al. 2004). Twelve of these sources have measured parallaxes from Dahn et al. (2002); Tinney, Burgasser & Kirkpatrick (2003); and Vrba et al. (2004); and 17 have proper motion measurements (although several did not at the time *HST* images were obtained; see below). Program GO-10247 targeted the peculiar T1 dwarf 2MASS 0518-2828 (Cruz et al. 2004), a source suspected of being multiple due to its peculiar near infrared spectrum. A compilation of the observed properties of all of the sources is provided in Table 1.

### 2.2. Imaging and Data Reduction

Table 2 provides a log of our *HST* observations. Each target was imaged over one orbit in the three filters F090M (except SDSS 1254-0122), F110W and F170M using the highest-resolution camera NIC1 (pixel scale 0".043, field of view 11"×11"). 2MASS 0518-2828 was also observed with the F145M and F160W filters. The F110W and F170M filters sample the peak spectral flux of T dwarfs (around 1.2  $\mu$ m) and the 1.6  $\mu$ m CH<sub>4</sub> band, respectively, as illustrated in Figure 1. As the near infrared CH<sub>4</sub> bands are primary classification diagnostics for T dwarfs (Burgasser et al. 2006a), F110W-F170M color can provide a rough estimate of spectral type (cf. § 3.2) as well as a discriminant for bona-fide, low-temperature brown dwarf companions. The F090M filter samples the red wing of the pressure-broadened 0.77  $\mu$ m K I doublet (Burrows, Marley, & Sharp 2000; Allard et al. 2003; Burrows & Volobuyev 2003), and provides an additional discriminant against background sources.

All data were acquired in MULTIACCUM mode. Multiple exposures in the F110W and F170M filters were obtained in a spiral dither pattern with steps of 1".3 ( $\sim 30$  NIC1 pixels). Total integration times in these two filters ranged over 791-912 s and 1519-1600 s, respectively, for the majority of our sample. Exceptions include 2MASS 0348-6022, which was observed for a longer period due to its location in the *HST* continuous viewing zone; and 2MASS 0518-2828, where shorter exposures were taken to allow observations in five filters over one orbit. Short (48-88 s), single F090M exposures were obtained for the GO-9833 targets. Multiple F090M, F145M and F160W exposures were obtained for 2MASS 0518-2828 using the same dither pattern as the F110W and F170M observations.

Several of our targets were not well centered on the

<sup>10</sup> We use abbreviated notation for sources in our observed sample throughout the text; e.g., 2MASS hhmm±ddmm, where the suffix is the J2000 sexagesimal Right Ascension (hours and minutes) and declination (degrees and minutes). Full source names and coordinates are provided in Table 1.

NIC1 camera due largely to their uncertain or unknown proper motions at the time of the observations. The most extreme case is that of 2MASS 0727+1710. At the time of the *HST* observations the proper motion of 2MASS 0727+1710 had not been measured, so the telescope was pointed at the 1997.83 epoch position as measured by 2MASS. Unfortunately, this source has one of the largest proper motions in our sample,  $1''.297 \pm 0''.005$  (Vrba et al. 2004), and the resulting  $8''.3$  motion between the 2MASS and *HST* imaging epochs was sufficient to move 2MASS 0727+1710 out of the NIC1 field of view. Observations of SDSS 0151+1244 were also offset due to source motion, and the object was imaged in the corner of the NIC1 camera’s field of view ( $1''.2$  from the closest edge of the array), limiting the area sampled for companions. The remaining sources were detected sufficiently close to the center of the NIC1 array ( $>2''.5$  from the array edge) to provide adequate sampling of separations within the resolution of the original discovery surveys ( $\sim 1''.5$ – $2''$  for SDSS and 2MASS).

Images were reduced by standard pipeline processing (CALNICA, Bushouse et al. 1997) using updated calibration images and photometric keywords as of August 2004. CALNICA reduction includes analog-to-digital correction, subtraction of bias and dark current frames, linearity correction, correction for readout artifacts (the “bars” anomaly), division by an appropriate flat field image, photometric calibration, cosmic ray identification, and combination of MULTIACCUM frames into a single calibrated image. Post-CALNICA processing was limited to the cleaning of cosmic rays and persistent bad pixels by nearest-neighbor interpolation, and the mosaicking of the F110W and F170M dithered image sets (and all five filter sets of 2MASS 0518-2828) using the CALNICB routine.

### 2.3. Resolved Sources

Subsections ( $2''.5 \times 2''.5$ ) of the reduced F090M, F110W and F170M mosaic images for each source are shown in Figure 2. North/east orientations are indicated by arrows, and the images are scaled logarithmically to highlight low flux features. Note the clearly resolved PSFs in most of the F110W and F170M images, resulting in significant structure outside of the core of the PSF including first-order Airy rings and diffraction spikes at wider separations. Three sources immediately stand out as obvious doubles. The previously reported binary SDSS 0423-0414 (Burgasser et al. 2005b) shows two overlapping PSFs roughly oriented along a NNE/SSW axis, with the northern component appearing to be slightly fainter in the F110W and F170M bands. SDSS 1021-0304 also appears to be a close double aligned along a ENE/WSW axis, with the western component appearing to be fainter at both F090M and F170M, but not F110W. 2MASS 1553+1532 is a well-resolved pair aligned along a N/S axis, with the southern component appearing to be slightly fainter at F090M (it is marginally detected in this band), F110W and F170M. This source had previously been reported as a candidate binary by Burgasser, Kirkpatrick & Brown (2002).

In addition to these three sources, PSFs of 2MASS 0518-2828 and 2MASS 0926+5847 are slightly elongated in the *HST* images and therefore also appear to be double. These sources are shown in more detail in Figure 3,

which displays contour plots of the central  $0''.9 \times 0''.9$  regions of the F090M and F110W images around 2MASS 0518-2828 and SDSS 0926+5847, respectively, and equivalent data for the unresolved source 2MASS 1503+2525. 2MASS 0518-2828 is slightly elongated along a N/S axis (PSF full width at half maximum of 1.86 pixels, as compared to 1.57 pixels for 2MASS 1503+2525), with the shape of its southern extension indicating a fainter component. All three F090M images obtained for 2MASS 0518-2828 show the same elongation in the same orientation, lending confidence to its reliability. The elongation is less obvious in the F110W and F145M images of this source, and marginally detected in the F160W and F170M images, presumably because it is obscured by the broader PSF at these wavelengths. SDSS 0926+5847 is clearly elongated along a NW/SE axis (PSF FWHM of 2.67 pixels at F110W, versus 2.06 pixels for 2MASS 1503+2525), and appears to be more symmetric, suggesting near-equal brightness components. Again, the same elongation is seen in each of the F110W and F170M exposures (the source is only marginally detected at F090M). We therefore conclude that both systems are resolved doubles. PSF fits for all of the doubles are presented in § 4. The remaining 17 targets appear to be single at the resolution of the NIC1 camera.

## 3. NICMOS PHOTOMETRY

### 3.1. Measurements

Aperture photometry for all of the sources in our sample were measured from the individual calibrated images using the IRAF<sup>11</sup> PHOT routine. Various aperture radii ranging from 2-20 pixels ( $0''.086$ – $0''.86$ ) about the source flux peak were examined, with a common background annulus of 20-30 pixels ( $0''.86$ – $1''.3$ ). Integrated source count rates were converted to photometric magnitudes on the Arizona Vega system ( $M_{Vega} = 0.02$ ) using the photometric keyword parameter PHOTFNU and Vega fluxes of 2157.3, 1784.9 and 946.1 Jy at F090M, F110W and F170M, respectively (Schultz et al. 2005). Individual magnitudes from dithered exposure frames were averaged to derive a single photometric measurement for each source. F145M and F160W magnitudes for 2MASS 0518-2828 were similarly measured using Vega fluxes of 1197.1 and 1042.6 Jy, respectively.

Aperture corrections in the F110W and F170M filters were determined from observations of the three highest signal-to-noise (S/N) single sources in our sample, 2MASS 0348+6022, SDSS 1254-0122 and 2MASS 1503+2525. Comparison of integrated flux profiles as a function of aperture size between these sources demonstrates excellent agreement, with deviations of less than 0.01 mag for apertures wider than 4 pixels. For F090M observations, we adopted aperture corrections measured from observations of 2MASS 0518-2828, even though this source is slightly resolved (all other sources have insufficient S/N in this filter). Table 3 lists the aperture corrections obtained for each filter, corrected from an 11.5 pixel ( $0''.49$ ) reference aperture to an infinite aperture using values from Schultz et al. (2005).

<sup>11</sup> IRAF is distributed by the National Optical Astronomy Observatories, which are operated by the Association of Universities for Research in Astronomy, Inc., under cooperative agreement with the National Science Foundation.

Photometric measurements are listed in Table 4. For unresolved sources and the marginally resolved pairs SDSS 0926+5847 and 2MASS 0518-2828, we report 5-pixel ( $0''.22$ ) aperture photometry corrected to an infinite aperture using the values in Table 3. For the resolved doubles SDSS 0423-0414 and SDSS 1021-0304, we report 15-pixel ( $0''.65$ ) aperture photometry encompassing both components with no aperture correction. This aperture size was chosen as it includes  $>90\%$  of the light in all three filters and minimizes photometric noise. For the well-resolved double 2MASS 1553+1532, we report corrected 3-pixel ( $0''.13$ ) aperture photometry for each component separately. Uncertainties include contributions from the scatter of individual measurements (typically 1-2%) and in the aperture corrections ( $<1\%$  for F110W and F170M, 5% for F090M), as well as 5% absolute calibration uncertainties and 1% zeropoint drift (Schultz et al. 2005). The 5% calibration uncertainties, which dominate the error budgets for F110W and F170M magnitudes, are highly correlated and reduce to 3% for NICMOS colors; e.g., F110W-F170M. These values are reported separately in Table 4. For 2MASS 0518-2828, we also measured  $F145M = 15.86 \pm 0.05$  and  $F160W = 15.20 \pm 0.05$ .

Formal limiting magnitudes for each source field and filter were determined by PSF simulation. Scaled PSFs of 2MASS 1503+2525 were added onto blank regions of the individual F090M, F110W and F170M exposures and checked for visual detection. Reliable detections were possible for peak flux scalings of 7, 5 and 5 times the background noise at F090M, F110W and F170M, respectively. These limits are given in Table 2. There is a slight correlation of these limiting magnitudes with telescope pointing angle with respect to the Moon, likely the result of increased background emission. Several of our sources were detected in the F090M exposures at magnitudes below the formal detection limits, and have appropriately poorer S/N.

### 3.2. T Dwarf Colors

The original motivation for the filter set employed in this study was to provide adequate color discrimination of bona-fide companions from coincident background sources, and to determine photometric classifications. Figure 4 compares F110W-F170M colors to spectral type for sources in our sample and unresolved late-type L dwarfs observed in the *HST* NICMOS program of Reid et al. (2006a). Spectral types are based on optical spectroscopy for the L dwarfs and near infrared spectroscopy for the T dwarfs. We also show synthetic colors measured from low resolution near infrared spectra of late-type L and T dwarfs from Burgasser et al. (2006a). Earlier than type T1, F110W-F170M color is relatively constant at  $\sim 1.8$  mag, albeit with significant dispersion ( $\pm 0.3$  mag) that is larger than the photometric uncertainties. For subclasses T1 and later, there is a tight correlation between spectral type and color. A linear fit to the photometric data for unresolved sources yields

$$SpT = 7.26 - 3.44(F110W - F170M) \quad (1)$$

(where  $SpT(T1) = 1$ ,  $SpT(T5) = 5$ , etc.), with an RMS scatter of 0.4 subclasses. Thus, F110W-F170M is a reliable proxy for spectral type in the T dwarf regime. F090M-F110W color also provides a gross discriminant

of T spectral type, as shown in Figure 5. These colors redden from 1.25 to 2.55 over spectral types T1 to T8, due largely to increased absorption by K I. However, photometric uncertainties are much larger for the F090M data, reducing its utility. We therefore focus on the F110W-F170M colors for our analysis.

Despite the apparent utility of *HST* colors to distinguish and classify T dwarfs, the vast majority of photometric data for these objects are from ground-based studies based principally on the *J* ( $1.2 \mu\text{m}$ ), *H* ( $1.6 \mu\text{m}$ ) and *K* ( $2.0 \mu\text{m}$ ) telluric opacity windows. To put our photometry into context with existing data, we compared *F110W* and *F170M* magnitudes to *J* and *H* photometry, respectively, on the 2MASS and Mauna Kea Observatory (MKO; Simons & Tokunaga (2002); Tokunaga, Simons & Vacca (2002)) systems. MKO data were collated from Leggett et al. (2002); Knapp et al. (2004); and references therein<sup>12</sup>. Figure 6 compares *J*-*F110W* and *H*-*F170M* colors to F110W-F170M color for T dwarfs in our sample. We also plot MKO/NICMOS synthetic colors derived from low resolution near infrared spectroscopy (from Burgasser et al. 2006a) as a comparison. There is a marked difference between 2MASS and MKO *J*-*F110W* colors. The former are roughly constant ( $\sim -0.75$  mag) for  $-0.2 \leq F110W - F170M \leq 1.7$ , but there is significant scatter ( $\sim 0.2$  mag) due primarily to the large uncertainties associated with faint 2MASS T dwarf photometry (typically 0.04-0.10 mag). In contrast, MKO *J*-*F110W* colors show a tight correlation with F110W-F170M color (MKO photometric uncertainties are typically 0.03-0.05 mag) and a 0.2-0.3 magnitude offset from 2MASS *J*-*F110W* colors due to differences in the filter profiles (cf. Stephens & Leggett 2004). A polynomial fit to the MKO/NICMOS photometric data for unresolved sources yields the relation

$$J_{MKO} - F110W = -1.15 + 0.025(F110W - F170M) + 0.035(F110W - F170M)^2 \quad (2)$$

with a scatter of 0.04 mag. 2MASS and MKO *H*-*F170M* colors are similar (the result of their equivalent *H*-band filter profiles), and both span a wider range than *J*-*F110W* colors due to strong  $1.6 \mu\text{m}$   $\text{CH}_4$  absorption in the later-type T dwarfs. *H*-*F170M* color is also correlated with F110W-F170M color, and a fit to MKO photometry for unresolved sources yields

$$H_{MKO} - F170M = -0.75 + 0.89(F110W - F170M) - 0.27(F110W - F170M)^2 \quad (3)$$

with a scatter of 0.05 mag. Interestingly, the combined light colors of SDSS 1021-0304 fall well off both of these lines. As discussed in § 5.3, these discrepancies are due to the unique composition of the SDSS 1021-0304 system. Note that equivalent relations for 2MASS/NICMOS photometry are presented in Reid et al. (2006a).

In Figure 7 we plot derived F110W and F170M bolometric corrections (BC) for T dwarfs in our sample as a function of F110W-F170M color. These were computed from ground-based MKO photometry and *K*-band BCs from Golimowski et al. (2004) as, e.g.,  $BC_{F110W} = BC_K + K_{MKO} - F110W$ . Again, there is good correlation between the NICMOS BCs and F110W-F170M

<sup>12</sup> A compilation of these data is maintained by S. Leggett at [http://www.jach.hawaii.edu/\\$\sim\\$sim\\$sk1/LTdata.html](http://www.jach.hawaii.edu/$\sim$sim$sk1/LTdata.html).

color, and a polynomial fit to the F110W photometry of unresolved sources yields

$$BC_{F110W} = 1.43 + 0.11(F110W - F170M) - 0.24(F110W - F170M)^2 \quad (4)$$

with a scatter of 0.07 mag.

#### 4. PSF FITTING

##### 4.1. Method

The properties of the five resolved doubles in our sample were determined by fitting individual images to PSF models using an algorithm similar to that described in Burgasser et al. (2003c). One important modification in this study was the use of model PSFs generated by the Tiny Tim program<sup>13</sup> (Krist 1995). Tiny Tim was specifically designed to generate PSFs for *HST* imaging data, and includes mirror zonal errors and filter passband effects in the model PSF shape. We generated several grids of Tiny Tim PSFs for the F090M, F110W and F170M filters appropriate for the post-cryocooler NICMOS NIC1 detector, sampling 169 positions across the chip in row/column increments of 16 pixels. For each calibration image, our PSF fitting routine employed the model PSF located closest to the position of the target on the chip. We also used near infrared spectral data for SDSS 1021-0304 from Burgasser et al. (2006a) as input to the Tiny Tim program in order to model the appropriate spectral response across the passband. Model PSFs were sampled at 10 times the native pixel resolution of NIC1 for subpixel shifting.

PSF fits were made for  $2''.5 \times 2''.5$  subsections of each image centered on the target sources, and initial guesses for the pixel positions and fluxes of the two components were made using a simple peak detection algorithm (for the primary) and single-PSF subtraction (for the secondary). Model images were then generated using two Tiny Tim PSFs resampled to the resolution of the data and scaled to the estimated peak fluxes of the detected sources. Our routine then iteratively searched for the optimal solution to the primary position, secondary position, primary flux and secondary flux, in that order, by computing the residuals between the model image and the data. Positional shifts of 0.1 pixels were made by shifting the oversampled model PSFs in integer units, and then downsampling to the resolution of the data. Fluxes were varied in steps of 1% (0.01 mag). The PSF fits were done recursively for convergence; i.e., if better solutions to any of the four binary parameters were found, the routine retested all of the parameters starting with the primary position until no reduction in residuals could be made.

Figure 8 illustrates the quality of these fits for one of the F170M images of the SDSS 1021-0304 pair. Shown are surface plots of the original data on a logarithmic vertical scale (to bring up the background noise), the best-fit PSF model, the result of subtracting the primary PSF model from the data, and the result of subtracting the full PSF model from the data. The primary-subtracted image shows a well-resolved secondary component, with clear detection of that component's first-order Airy ring. The final subtraction is extremely clean

and average residuals (typically  $<1\%$  of the peak source flux for all fits) are at the level of background noise.

Final estimates of the flux ratio, separation and position angles of each double were determined as the mean of individual determinations from each calibrated image, with some vetting of very poor fits caused largely by cosmic ray hits close to the target source. Uncertainties include scatter in the individual fits and systematic uncertainties of 0.01 mag and  $0''.004$  in flux ratio and separation, respectively, as prescribed by the fitting routine. These values are listed in Table 5

For the wider doubles SDSS 0423-0414, SDSS 1021-0304 and 2MASS 1553+1532, we estimate that additional systematic effects in the fitting process are insignificant given the well-resolved nature of these sources and minimal residuals. Indeed, resolved aperture photometry for the 2MASS 1553+1532 pair are consistent with the PSF results within measured uncertainties. For the closer binaries 2MASS 0518-2828 and SDSS 0926+5847, whose angular separations are less than 2 NIC1 pixels, systematic effects may be more important. To examine this possibility, we experimented with PSF fits to test data constructed to mimic the measured properties of the 2MASS 0518-2828 and SDSS 0926+5847 pairs in the F110W and F170M bands. A total of 300 test images were constructed for each target/filter simulation using random pairings of  $2''.5 \times 2''.5$  subsections of images for the brightest unresolved sources in our sample (2MASS 0348-6022, SDSS 1254-0122 and 2MASS 1503+2525, for a total of 23 PSF images at F110W and 13 PSF images at F170M). The selected PSF images were shifted by subpixel resampling to replicate separations and position angles randomly drawn from Gaussian distributions centered at the measured values of the binary under investigation, and with distribution widths twice the measured uncertainties. The secondaries in each test image were scaled to a flux ratio randomly drawn from a uniform distribution (in magnitude space) spanning 0 mag to the measured magnitude difference plus three times the measured uncertainty. These test images were then run through the same PSF fitting algorithm as described above to derive experimental values. Systematic effects were ascertained by selecting only those test cases where the experimental values agreed with the measured values for the binaries, and then computing the mean and standard deviation of the associated input parameters. For 2MASS 0926+5847, these simulations indicate that the underlying flux ratios for this system ( $\Delta F110W^{(sim)} = 0.4 \pm 0.2$ ,  $\Delta F170M^{(sim)} = 0.4 \pm 0.3$ ) are closer to unity, as suggested by visual inspection of the images themselves (cf. Figure 3). Similar systematic flux ratio offsets are indicated for 2MASS 0518-2828 ( $\Delta F110W^{(sim)} = 0.8 \pm 0.5$ ,  $\Delta F170M^{(sim)} = 0.9 \pm 0.6$ ). The flux ratio offsets are largely due to the PSF fitting algorithm attempting to fit both components with a single PSF, while the secondary PSF fits the largest peak in the residuals. There were no indications of systematic offsets in the separations or position angles of these systems, however. The “systematics-corrected” flux ratios resulting from these simulations are given in Table 5.

<sup>13</sup> See <http://www.stsci.edu/software/tinytim/tinytim.html>.

The angular separations of our sources range from  $0''.051 \pm 0''.012$  (2MASS 0518-2828) to  $0''.349 \pm 0''.005$  (2MASS 1553+1532). Assuming spectrophotometric distance estimates for 2MASS 0518-2828, SDSS 0926+5847 and 2MASS 1553+1532 of  $34 \pm 6$ ,  $38 \pm 7$  and  $12 \pm 2$  pc based on their combined light 2MASS  $J$ -band magnitudes (corrected for equal-brightness components) and the  $M_J$ /spectral type relations of Tinney, Burgasser & Kirkpatrick (2003), projected separations range over 1.8-5.0 AU. These values are consistent with the small separations typically found for resolved brown dwarfs (Burgasser et al. 2006b).

Relative magnitudes and combined light photometry were used to determine component F110W and F170M magnitudes and colors; these are also listed in Table 5. For SDSS 0423-0414, SDSS 1021-0304 and 2MASS 1553+1532, the secondary colors are consistent with T dwarf spectral types of T2, T5 and T7, respectively. Component colors for SDSS 0926+5847 (after correction for systematic effects) indicate spectral types of  $T4 \pm 0.5$ , consistent with the composite spectral type of T4.5. Component colors for 2MASS 0518-2828 have much larger uncertainties, and we can only ascertain that they are consistent with spectral types  $\sim T3$  and earlier. In all cases, we can rule out that the secondaries are hotter background stars, since both component and composite F090M magnitudes would be significantly brighter than observed. Furthermore, the likelihood of a background source lying near any of the target sources is very small. In our entire sample, only five additional point sources were detected at F110W in the  $11''^2$  NIC1 field of view, with magnitudes of 19.5-22.5. Assuming that the background surface density scales as  $10^{0.6F_{110W}}$  (i.e., scaling as  $d^3$ ), then the probability of a background source with F110W  $\lesssim 18.0$  mag (bracketing the estimated magnitudes of the detected secondaries) lying within  $1''$  of any target source is  $5 \times 10^{-6}$ , and can be ruled out at the  $>4\sigma$  confidence level. We therefore conclude that all five secondaries are physically bound T dwarf companions.

Utilizing our derived F110W bolometric correction/color relation (Eqn. 4), we can determine the relative bolometric luminosities of the binary components as

$$\begin{aligned} \Delta M_{bol} &\equiv M_{bol}(B) - M_{bol}(A) \\ &= \Delta F_{110W} + BC_{F_{110W}}(B) - BC_{F_{110W}}(A) \end{aligned} \quad (5)$$

These values are given in Table 5. We also list absolute  $M_{bol}$  values for the components of SDSS 0423-0414 and SDSS 1021-0304, which have parallax distance measurements. In all cases, we verify that the secondaries are less luminous than the primaries, as expected. Relative effective temperatures,  $T_B/T_A$ , were determined from the relative bolometric luminosities assuming identical component radii, so that  $T_B/T_A = (L_B/L_A)^{1/4}$ . Again, secondary  $T_{effs}$  are less than primary  $T_{effs}$  for all five systems, although in no case are differences more than  $\sim 20\%$ . These ratios are consistent with estimated component  $T_{effs}$  based on their spectral types (from F110W-F170M color and spectral decomposition; see § 5.3) and the  $T_{eff}$ /spectral type relation of Golimowski et al. (2004), taking into account the 124 K scatter in the latter relation. For SDSS 0423-0414 and SDSS 1021-0304,

we derived component  $T_{effs}$  from their individual luminosities and assumed radii of  $0.095 \pm 0.010 R_\odot$ , appropriate for 0.5-5 Gyr brown dwarfs in the  $T_{eff}$  range of late-type L and T dwarfs (Burrows et al. 1997). These effective temperatures are consistently 100-200 K lower than those based on the Golimowski et al. (2004) relation. Although the deviations are comparable to the uncertainties in both this relation and our  $T_{eff}$  determinations, the Golimowski et al. (2004) results may be overestimated in this spectral type regime due to contamination by these previously unresolved (and hence overluminous) binaries.

Finally, we derived mass ratios for the five binary systems, assuming coequality, using the mass-luminosity power-law relation of Burrows et al. (2001),  $L \propto M^{2.64}$ , implying

$$q \approx 10^{\frac{-\Delta M_{bol}}{6.6}}. \quad (6)$$

System mass ratios are all 0.7 or greater, similar to most currently known brown dwarf pairs. Individual component masses were estimated from the evolutionary models of Burrows et al. (1997) using the component  $T_{effs}$  (for 2MASS 0518-2828, SDSS 0926+5847 and 2MASS 1553+1532) or  $M_{bols}$  (for SDSS 0423-0414 and SDSS 1021-0304), and assuming an age range of 0.5-5 Gyr, typical for local disk dwarfs (Reid & Hawley 2000). These component masses are roughly consistent with the estimated mass ratios. Orbital period estimates were derived assuming circular orbits and semimajor axes  $a \approx 1.26\rho$  (Fischer & Marcy 1992). These periods range over 10-50 yr, with the SDSS 0423-0414, 2MASS 0518-2828 and SDSS 0926+5847 systems ( $P \lesssim 20$  yr) appearing to be the best targets for dynamical mass measurements.

### 4.3. Search Limits for Very Faint Companions

In order to search for even fainter companions to unresolved T dwarfs in our sample, we repeated the PSF fitting analysis described above on the F110W calibrated images using a single PSF model for the primary. The F110W images were chosen because this filter samples the peak of the near infrared spectral flux of brown dwarfs down to  $T_{eff} \approx 500$  K (Burrows, Sudarsky & Lunine 2003), and therefore provides the most sensitive probe for low mass companions. We examined residual images (subtraction of the PSF model from the data) by eye for faint point sources that persist in the same location relative to the original primary. Out of the entire sample, only one ‘‘candidate’’ companion was identified, a faint source (F110W  $\approx 22.0$ ) located  $0''.97$  northeast of the T1 SDSS 0151+1244. This source has a high probability of being spurious, however; it does not appear in either the F090M or F170M images, and due to the pointing offset of the *HST* observations of SDSS 0151+1244 (see § 2.2) was only detected in one F110W exposure. While it is therefore likely to be a residual cosmic ray or ghost, it warrants follow-up confirmation imaging since its brightness relative to SDSS 0151+1244 is consistent with a  $T_{eff} \sim 450$  K brown dwarf companion.

Sensitivity limits for putative faint companions were quantified by examining the F110W radial profiles for each of the unresolved sources before and after PSF subtraction. Examples of the brightest (2MASS 1503+2525) and faintest (SDSS 0207+0000) sources are shown in Fig-

ure 9. PSF subtraction results in residuals that are  $\sim 4$ - $4.5$  mag fainter than the peak source flux in the core and first Airy ring ( $\rho \lesssim 0''.2$ ), irrespective of the brightness of the primary. At larger separations, there is little or no improvement in sensitivity beyond the inherent decrease in the primary flux, and residuals are largely background limited at  $\rho \gtrsim 0''.4$ . Faint source sensitivity limits (assuming  $3\sigma$  detections) for each of the unresolved sources, including mass ratio limits assuming  $\Delta F_{110W} \sim \Delta M_{bol}$  and using Eqn. 6 are given in Table 6. These detection limits can be characterized as follows:

- No detections for  $\rho \lesssim 0''.04$ ,
- $\Delta F_{110W} \sim 3$ - $3.5$  mag ( $q \gtrsim 0.3$ - $0.4$ ) for  $0''.04 \lesssim \rho \lesssim 0''.2$ ,
- $\Delta F_{110W}$  varying from  $\sim 3$ - $3.5$  mag to the background limit ( $\sim 4$ - $6.5$  mag;  $q \gtrsim 0.1$ - $0.3$ ) for  $0''.2 \lesssim \rho \lesssim 0''.4$ , and
- $\Delta F_{110W}$  background limited for  $\rho \gtrsim 0''.4$ .

Assuming all of our sources have masses below the hydrogen burning minimum mass ( $\sim 0.075 M_{\odot}$ ; Chabrier et al. 2000; Burrows et al. 2001), these observations rule out companions down to just above the deuterium burning limit ( $\sim 0.012 M_{\odot}$ ; Burrows et al. 2001) for most of our targets.

Finally, we comment on the 5 faint sources ( $F_{110W} = 19.5$ - $22.5$ ) detected at wider separations ( $\rho \gtrsim 4''$ ) in the NIC1 images. These can be ruled out as low temperature companions based on their magnitudes and  $F_{110W}$ - $F_{170M}$  colors, typically  $1.2$ - $1.4$  mag, inconsistent with co-spatial mid- and late-type T dwarf companions but typical for background M stars.<sup>14</sup> We conclude that no bona-fide companions are present around any of our targets with  $\rho \gtrsim 0''.4$  and  $q \gtrsim 0.1$ - $0.3$ .

## 5. ANALYSIS OF INDIVIDUAL SOURCES

### 5.1. *SDSS 0423-0414*

The identification of SDSS 0423-0414 as a binary system was previously reported in Burgasser et al. (2005b). The parameters reported here supersede those of the previous paper, although all measurements are consistent within the reported uncertainties. This source, similar in composition to the recently resolved binary 2MASS J22521073-1730134 (Reid et al. 2006b), is an unusual system, as its combined light optical spectrum (Cruz et al. 2003, Kirkpatrick et al. in prep.) exhibits both  $6563 \text{ \AA}$   $H\alpha$  emission, an indicator of magnetic activity; and  $6708 \text{ \AA}$  Li I absorption, present in brown dwarfs with masses below the Li-burning minimum mass ( $\sim 0.065 M_{\odot}$ ; Rebolo, Martín, & Magazzu (1992)). Both signatures are rare in very late-type L dwarfs and T dwarfs, as the strength and frequency of  $H\alpha$  emission plummets across the L dwarf regime (Gizis et al. 2000; Kirkpatrick et al. 2000; Mohanty & Basri 2003; West et al. 2004), while Li I absorption becomes increasingly difficult to detect against a progressively fainter

continuum suppressed by pressure-broadened Na I and K I lines (Burrows & Volobuyev 2003). The only other sources known to exhibit the same combination of features are the L2 Kelu 1 (Ruiz, Leggett, & Allard 1997), which has also been resolved as a binary system (Liu & Leggett 2005; Gelino, Kulkarni & Stephens 2006); the L0.5 2MASS J20575409-0252302 (Cruz et al. 2003), which has not (Reid et al. 2006a); and the L0 2MASS J11544223-3400390 (Kirkpatrick et al., in prep.), which has not yet been imaged at high angular resolution.

This raises the question: from which component or components do these spectral features arise? Decomposition of the combined light near infrared spectrum using the resolved NICMOS photometry indicates that this system is composed of an L6.5 primary and a T2 secondary (Burgasser et al. 2005b, see § 5.3).  $H\alpha$  emission from T dwarfs is rare; only three other T dwarfs have been detected in emission (Burgasser et al. 2003a), one of which, 2MASS J12373919+6526148 (Burgasser et al. 1999), is unusually active and is speculated to be a very tight ( $\rho \sim 0.1 R_{\odot}$ ) interacting binary system (Burgasser et al. 2000a, 2002a). The  $H\alpha$  line flux as measured from combined light optical spectral data (Kirkpatrick et al. in prep.), flux calibrated to SDSS  $i'$  photometry ( $20.22 \pm 0.04$ ; Geballe et al. 2002), is  $1.7 \times 10^{-17}$  ergs  $\text{cm}^{-2} \text{ s}^{-1}$ . Using the component bolometric luminosities listed in Table 5, we derive  $\log L_{H\alpha}/L_{bol} = -5.5$  if the emission arises from the L6.5 primary, and  $-5.2$  if it arises from the T2 secondary. Compared to similar-typed objects exhibiting  $H\alpha$  emission – e.g., DENIS-P J0205.4-1159 (L7;  $\log L_{H\alpha}/L_{bol} < -6.2$ ; Mohanty & Basri 2003) and SDSS 1254-0122 (T2;  $\log L_{H\alpha}/L_{bol} = -5.8$ ; Burgasser et al. 2003a) – the emission flux from either component is not necessarily extreme, but is nevertheless rare in this spectral type regime (cf. Figure 3 in Burgasser et al. 2002a).

Turning to the  $6708 \text{ \AA}$  Li I line, Liu & Leggett (2005) have pointed out that the detection of this feature in a substellar binary can be used as a powerful constraint of systemic age in conjunction with theoretical evolutionary models, particularly if the absorption can be attributed to one or both components. SDSS 0423-0414 exhibits a prominent Li I line, and as luminous flux in this spectral region is dominated by the earlier-type primary (the optical classification of this source is L7.5; Cruz et al. 2003) it is likely that this component is responsible for the absorption. This deduction is supported by the fact that atomic Li gas is likely to be depleted in the photosphere of the secondary (for which we derive  $T_{eff} = 1260 \pm 70 \text{ K}$ ) as Li is incorporated into LiCl and LiOH at  $T_{eff,S} \lesssim 1500 \text{ K}$  and pressures  $\gtrsim 1$ - $10$  bar (Lodders 1999).

Assuming then that the observed absorption arises from the L6.5 primary, which must then have  $M \lesssim 0.065 M_{\odot}$ , an upper age limit of  $1.7 \text{ Gyr}$  can be deduced using the theoretical evolutionary models of Burrows et al. (1997); this is illustrated in Figure 10. This age is on the young side for a field dwarf, and may explain the presence of  $H\alpha$  emission in one or both components; observations of fully-convective lower main sequence stars in the field and clusters shows that magnetic activity is commonly enhanced in young stars (Hawley et al. 1999; Reid 2003).

<sup>14</sup> The most interesting source is located  $7''.63$  northeast of SDSS 1254-0122 at  $12^h 54^m 54^s 14 - 01^d 22' 42'' 84$ . With  $F_{110W}$ - $F_{170M} = 2.31 \pm 0.14$ , this source is likely to be a highly reddened background star or faint unresolved galaxy.

It is also consistent with the kinematics of this system, as its tangential velocity,  $V_{tan} = 24.0 \pm 0.7 \text{ km s}^{-1}$ , is on the low end of the T Dwarf  $V_{tan}$  distribution of Vrba et al. (2004). An estimated minimum age for this system of 0.5 Gyr can be argued from the absence of low surface gravity features in its combined-light optical spectrum (e.g., VO absorption and weakened alkali lines; see Kirkpatrick 2005). Thus, the components of SDSS 0423-0414 are among the few brown dwarfs with well-constrained ages, distances and bolometric luminosities.

### 5.2. 2MASS 0518-2828

The detection of a companion to 2MASS 0518-2828 appears to confirm the binary hypothesis of Cruz et al. (2004) for this source, put forth to explain its unusual near infrared spectrum. 2MASS 0518-2828 exhibits clear  $\text{CH}_4$  absorption at  $1.6 \mu\text{m}$  but no  $\text{CH}_4$  band at  $2.2 \mu\text{m}$ . This is in contrast with trends in the standard L/T spectral sequence, where the  $2.2 \mu\text{m}$  band is seen to develop in the latest-type L dwarfs first, followed by  $1.6 \mu\text{m}$  absorption at the start of the T sequence (Geballe et al. 2002). Cruz et al. (2004) found that the combination of L6 and T4 spectra, with the latter scaled to be 20% brighter at  $1.27 \mu\text{m}$  adequately matches the observed spectral energy distribution for 2MASS 0518-2828. The small separation of this source, and the corresponding poor determination of its relative photometry, makes it impossible to verify the conjectured spectral types of the components based on these *HST* observations (although our photometry are consistent with these types). However, the fact that 2MASS 0518-2828 is resolved into two components makes this scenario likely.

### 5.3. SDSS 1021-0304

Like SDSS 0423-0414 and 2MASS 0518-2828, SDSS 1021-0304 appears to be a binary straddling the L/T transition, with component F110W-F170M colors indicating spectral types of  $\lesssim$ T2 and T5. However, this source is particularly interesting as the two components have nearly equal magnitudes at F110W, while the secondary is a full magnitude fainter at F170M. Because  $\text{H}_2\text{O}$  and  $\text{CH}_4$  absorption bands encompassed by the F110W filter bandpass (cf. Fig. 1) become stronger with later spectral types, the equivalent magnitudes of the two components suggests that the secondary has a brighter peak flux density, like 2MASS 0518-2828.

To explore this possibility, we performed a spectral decomposition of the combined light near infrared spectra of this source and SDSS 0423-0414 using a method similar to that described in Burgasser et al. (2005b) and Reid et al. (2006b). In brief, our technique involves the combination of various pairings of standard spectra (sources with well-defined classifications) after scaling them to the relative fluxes of the binary system under investigation. The hybrid spectra were then compared to the combined light spectrum of each (unresolved) binary to determine the best match. We performed our analysis on low resolution ( $\lambda/\Delta\lambda \sim 150$ ) near infrared data obtained with the SpeX spectrograph (Rayner et al. 2003) mounted on the 3.0m NASA Infrared Telescope Facility. Details on the acquisition, reduction and characteristics of these data are described in detail in Burgasser et al. (2004a, 2006a). The comparison basis set was composed of equivalent spectra of late L and T dwarf stan-

dards from Kirkpatrick et al. (1999); Cruz et al. (2003); and Burgasser et al. (2006a); specifically: 2MASS J08354256-0819237 (L5), 2MASS J04390101-2353083 (L6.5), DENIS-P J0205.4-1159<sup>15</sup> (Delfosse et al. 1997, L7), 2MASS J16322911+1904407 (L8), SDSS 0151+1244 (T1), SDSS 1254-0122 (T2), 2MASS 1209-1004 (T3), 2MASS 2254+3123 (T4), 2MASS 1503+2525 (T5) and SDSS 1624+0029 (T6). Pairings of the standard spectra were scaled to the observed F110W flux ratios, then added together and normalized. The quality of agreement between the resulting hybrid spectra and those of the binaries was quantitatively determined by comparison of the  $\text{H}_2\text{O}$ ,  $\text{CH}_4$  and  $K/J$  spectral indices defined in Burgasser et al. (2006a), as well as the relative F170M flux ratios between the spectral components.

The best matches for SDSS 0423-0414 and SDSS 1021-0304 are shown in Figure 11. For the former, we confirm previous results by Burgasser et al. (2005b), finding a best fit to a combination of the L6.5 2MASS 0439-2353 and the T2 SDSS 1254-0122. A hybrid spectrum of the T1 SDSS 0151+1244 and the T5 2MASS 1503+2525 provides the best match for SDSS 1021-0304. Note that the derived spectral types of the secondary components agree with photometric classifications based on F110W-F170M colors. In both cases the hybrid spectra show remarkable agreement with the binary spectra, both in terms of band strengths and the overall spectral energy distribution, across the full 0.8-2.5  $\mu\text{m}$  band. The relative F170M magnitudes as measured from the scaled component spectra are in rough agreement with *HST* photometry, differing by at most  $\sim 0.1$  mag, an offset attributable to the low resolution and calibration uncertainties in the spectral data.

Examining the relative fluxes of the best-fit component spectra for SDSS 1021-0304 in more detail, a remarkable fact is revealed. The emergent flux density of the T5 secondary of this system is 31% brighter than that of the T1 primary at the peak of the spectral energy distribution ( $1.27 \mu\text{m}$ ), and 24% brighter at the  $1.05 \mu\text{m}$  flux peak. This is despite the fact that the secondary is 11% cooler and 37% less luminous overall. That these spectral peaks differ significantly between the two components while F110W magnitudes are roughly equivalent can be explained by the redistribution of flux within the F110W bandpass. The increased brightening at  $1.05$  and  $1.27 \mu\text{m}$  in the secondary component is offset by deeper  $\text{H}_2\text{O}$  and  $\text{CH}_4$  bands at  $1.1$  and  $1.35 \mu\text{m}$ . At the bottom of these molecular features, and at shorter and longer wavelengths, the primary component is brighter. The components of SDSS 0423-0414 do not exhibit this same brightness inversion, although the peak flux densities are rather similar (differing by less than 25% at  $1.27 \mu\text{m}$ ) given the large differences in spectral type. The brightening of the secondary component of SDSS 1021-0304 is similar to that hypothesized for 2MASS 0518-2828, and more recently observed for the T1.5+T5.5 binary SDSS J153417.05+161546.1 (Liu et al. 2006, hereafter SDSS 1534+1615). Indeed, the photometric and spectroscopic

<sup>15</sup> DENIS-P J0205.4-1159 is either a resolved, near-equal mass binary (Koerner et al. 1999; Leggett et al. 2002) or a triple (Bouy et al. 2005), and is arguably a poor choice for this analysis. However, we did not have an alternate L7 comparison source, and DENIS-P J0205.4-1159 is currently the L7 optical spectral standard on the Kirkpatrick et al. (1999) scheme.

properties of SDSS 1021-0304 and SDSS 1534+1615 are quite similar. We discuss the observed  $J$ -band brightening, and its implications on the transition between L dwarfs and T dwarfs, in § 7.

#### 5.4. 2MASS 1217-0311

Burgasser et al. (2003c) reported a possible faint companion to this object in *HST* Wide Field Planetary Camera 2 imaging, but our NICMOS observations fail to reveal this source. Assuming that the relative flux at F110W between 2MASS 1217-0311 and the putative companion is as bright or brighter than that at F1042M ( $\lambda_c = 1.02 \mu\text{m}$ ), it would have been easily detected at the separation ( $0''.21$ ) and flux ratio (2.4 mag) previously observed. It is likely that the prior detection was an unfortunate combination of cosmic ray hits localized near the target source.

#### 5.5. 2MASS 1553+1532

2MASS 1553+1532 is the latest-type binary in our sample, and the best resolved. The F110W-F170M colors are consistent with very similar spectral types (T6.5 and T7), effective temperatures (within 7%) and masses ( $q = 0.90 \pm 0.02$ ). With a separation of  $0''.349 \pm 0''.005$  the 2MASS 1553+1532 pair is resolvable by ground-based imaging under the best seeing conditions, and was previously reported as a possible binary by Burgasser, Kirkpatrick & Brown (2002) based on imaging observations with the Keck 10m Near Infrared Camera (Matthews & Soifer 1994, hereafter NIRC) on 2000 July 22 (UT). We have revisited these data to determine whether the two components share common proper motion, and to search for orbital motion.

Conditions during the Keck observations in 2000 were particularly excellent, with clear skies and seeing of  $0''.3$  (full width at half maximum) at  $K_s$  during the observations. 2MASS 1553+1532 was observed in this filter, with 10 dithered exposures of 20s each obtained sequentially. Immediately following these observations, 10 dithered 20s exposures of the unresolved T dwarf 2MASS 2254+3123 were also obtained. Despite the large angular offset between the sources, we used these observations for PSF calibration as no other sufficiently bright and unresolved sources were detected in the 2MASS 1553+1532 fields. Raw images for both datasets were pairwise subtracted to eliminate first order background emission, and checked for linearity. No further reduction of the data (e.g., flat fielding) was done as relative photometry was not a priority. Figure 12 shows the PSFs of 2MASS 2254+3123 and 2MASS 1553+1532. The latter is clearly extended along a NNE/SSW axis, but the underlying components overlap substantially. We extracted astrometric information using a PSF fitting algorithm similar to that described above, but in this case comparing  $3'' \times 3''$  subsections of each pair-wise subtracted frame of 2MASS 1553+1532 to all 10 observations of 2MASS 2254+3123, for a total of 100 separate fits. Imposing the condition that average residuals be less than 3% of the peak source flux, the 42 best fits gave a mean separation  $\rho = 0''.30 \pm 0''.03$  (assuming a camera pixel scale of  $0''.153$ ) and position angle  $\theta = 199 \pm 7^\circ$ .

The difference in epoch between the *HST* and Keck images is 3.126 yr. A preliminary proper motion of this

object as measured by the USNO infrared parallax program (Vrba et al. 2004) of  $\sim 0''.4 \text{ yr}^{-1}$  (F. Vrba 2006, private communication) implies a total motion of the system of  $\sim 1''.3$  over this period. Yet the change in the relative separation between the two components is only  $0''.05 \pm 0''.03$ . These observations therefore confirm common proper motion for this pair, which are almost certainly gravitationally bound.

As for orbital motion, both the separation and position angle of this system have changed only slightly between the Keck and *HST* observations. While only marginally significant ( $\Delta\theta = 9 \pm 7^\circ$ ), Figure 13 illustrates that these slight changes are perceptible. However, the small position angle change is significantly less than that expected ( $\sim 26^\circ$ ) for its estimated 45 yr orbital period. This suggests that the true orbital period may be much longer, possibly due to smaller component masses in a younger system, or a particularly eccentric orbit; or that the orbital inclination is quite different from a face-on projection (consistent with the slight change in the separation of the two components). Further high-resolution imaging may constrain these possibilities in a reasonably short time period ( $\sim 5 \text{ yr}$ ), but mapping of the full orbit is clearly a long-term prospect.

## 6. AN UPDATED ASSESSMENT OF BROWN DWARF MULTIPLICITY

### 6.1. The Binary Fraction

The fraction of resolved binaries in our sample is  $\epsilon_b^{obs} = 5/22 = 23_{-6}^{+11}\%$ , where the uncertainties take into account the size of the sample (Burgasser et al. 2003c). This is similar to resolved binary fractions measured for other large high resolution imaging samples of VLM field dwarfs (Reid et al. 2001, 2006a; Bouy et al. 2003; Close et al. 2003; Gizis et al. 2003; Siegler et al. 2005). However, as all of these samples are largely magnitude-limited, this fraction is biased in favor of unresolved, near-equal mass ratio binaries. We can estimate the underlying (i.e., volume-limited) binary fraction,  $\epsilon_b$ , as (cf. Eqns. 4 and 5 in Burgasser et al. (2003c))

$$\epsilon_b = \frac{\epsilon_b^{obs}}{\alpha(1 - \epsilon_b^{obs}) + \epsilon_b^{obs}}, \quad (7)$$

where

$$\alpha \equiv \frac{\int_0^1 (1 + q^{2.64})^{3/2} f(q) dq}{\int_0^1 f(q) dq} \quad (8)$$

is the fractional increase in volume sampled for binaries with flux ratio  $f_B/f_A \approx q^{2.64}$  (Eqn. 6) and mass ratio distribution  $f(q)$ . In Burgasser et al. (2003c), both flat and delta-function forms of  $f(q)$  were considered; here, we explicitly calculate  $\alpha = 2.50_{-0.06}^{+0.04}$  using a power-law mass ratio distribution as described below. This yields  $\epsilon_b = 11_{-3}^{+7}\%$ , a value consistent with previous determinations of bias-corrected VLM binary fractions (Burgasser et al. 2003c; Close et al. 2003; Siegler et al. 2005) and volume-limited estimates (Bouy et al. 2003; Reid et al. 2006a,  $\sim 15\%$  and  $12_{-3}^{+7}\%$ , respectively).

It is important to stress that this fraction applies only to those binary systems that are resolvable by direct imaging. For our study, this limits the phase space sampled to  $\rho \gtrsim 1 \text{ AU}$  and  $q \gtrsim 0.35$ , or  $\rho \gtrsim 5 \text{ AU}$  and  $q \gtrsim$

0.2. The equivalent phase space of F-G and M dwarf binaries in the studies of Duquennoy & Mayor (1991) and Reid & Gizis (1997) yield binary fractions of 39% (combining both mass ratio and period distributions) and  $24_{-4}^{+6}\%$  (for  $M_V > 9$ ), respectively. Hence, in equivalent phase spaces the binary fraction of brown dwarfs in our sample is less than that of more massive stars.

But does this mean that the overall binary fraction of brown dwarfs is less? Maxted & Jeffries (2005) have proposed that a substantial fraction (50-67%) of VLM binaries may be hiding in more closely separated systems ( $\rho \lesssim 2.6$  AU) and can only be resolved as spectroscopic binaries. This projected separation corresponds to an angular separation of  $\lesssim 0''.13$  at the average distance of sources in our sample ( $\sim 20$  pc), only 3 NIC1 pixels. Indeed, over 25% of resolved brown dwarf binaries identified to date have angular separations below this limit, with the majority close to the resolution limits of *HST*. This supports the possibility that a significant number of more closely-separated and/or more distant systems remain unresolved. Bayesian statistical analysis of high resolution imaging studies by Reid et al. (2006a), which takes into account the possible presence of unresolved systems, indicates an overall VLM binary fraction of 24%, twice that of the resolved fraction.<sup>16</sup> This still places the binary fraction of VLM dwarfs at 1/3 that of solar-type stars, and 2/3 that of M dwarfs, consistent with a decreasing binary fraction toward later spectral types and lower masses.

### 6.2. The Separation Distribution

The projected separation distribution of 30 brown dwarf binaries resolved by high resolution imaging surveys to date are shown in Figure 14. These include systems listed in Burgasser et al. (2006b)<sup>17</sup> that have estimated primary masses below  $0.075 M_\odot$ . In accordance with previous studies, we find that this distribution peaks at very close separations,  $\sim 4$  AU with a broad peak spanning 2-8 AU. This is significantly lower than the 30 AU peak of the F-G and M binary separation distributions (Duquennoy & Mayor 1991; Fischer & Marcy 1992). Indeed, no brown dwarf field binaries have been identified with separations  $\gtrsim 15$  AU. However, two wider brown dwarf binaries systems have been recently identified in young cluster/associations: 2MASS J11011926-7732383 (Luhman 2004), a 240 AU binary in the  $\sim 2$  Myr Chameleon I association; and 2MASS J1207334-393254 (Chauvin et al. 2004, 2005), a 40 AU, very low mass ( $M_{tot} \sim 0.03 M_\odot$ ) brown dwarf binary in the  $\sim 8$  Myr TW Hydrae association (Gizis 2002). Both systems are very young, and it remains unclear as to whether their configurations are stable long-term (Mugrauer & Neuhäuser 2005). The widest VLM field binary so far identified, DENIS J055146.0-443412.2 (Billeres et al. 2005, 220 AU), is likely composed of two VLM stars. Hence, the wide sep-

<sup>16</sup> Note that this analysis assumes a symmetric Gaussian separation distribution; the fraction may be higher (lower) if there is an excess (deficiency) of short period systems (cf. Maxted & Jeffries 2005).

<sup>17</sup> This sample incorporates binaries identified in Martín et al. (1999); Leinert et al. (2001); Reid et al. (2001, 2006a); Potter et al. (2002); Bouy et al. (2003); Burgasser et al. (2003c); Gizis et al. (2003); McCaughrean et al. (2004); Burgasser et al. (2005a); Liu & Leggett (2005); Liu et al. (2006); and this study.

aration brown dwarf binary desert originally suggested by Martín et al. (2000) — not to be confused with the brown dwarf companion desert around solar-type stars (Marcy & Butler 2000) — remains a distinct characteristic of brown dwarf binaries in the field.

At closer separations, imaging surveys are limited by angular resolution. Hence, the true peak of the brown dwarf separation distribution may be lower than that inferred from Figure 14. Nevertheless, it is interesting to note that the separations of binaries identified in this survey — and indeed all T dwarf binaries identified to date — are  $\lesssim 5$  AU, such that most T dwarf binaries have separations below the peak of the brown dwarf distribution. The apparent compactness of T dwarf binaries as compared to warmer M- and L-type brown dwarf systems is consistent with a maximum binary separation that scales with total system mass (Reid et al. 2001; Burgasser et al. 2003c; Close et al. 2003), since cooler brown dwarfs have lower masses than warmer ones at a given age. However, the smaller separations of T dwarf binaries may also be due to selection effects. T dwarfs are intrinsically fainter and typically found at closer distances to the Sun than M and L dwarfs in magnitude-limited surveys. Hence, T dwarf binaries can generally be observed at higher linear resolution. A statistically robust volume-limited sample of M-, L- and T-type brown dwarfs would provide an adequate check for mass dependency in the separation distribution of substellar objects.

### 6.3. The Mass Ratio Distribution

The mass ratio distribution of brown dwarf binaries is shown in Figure 15. This distribution is clearly peaked at  $q \sim 1$ , with  $50 \pm 9\%$  of all known systems having near-equal mass components. Again, because the majority of these systems were originally selected from magnitude-limited surveys, there is an inherent bias in the discovery of equal-mass systems that scales approximately as  $(1 + q^{2.64})^{3/2}$ . A bias-corrected distribution, also shown in Figure 15, nevertheless shows that near-equal mass ratio systems are predominant. This result is robust even when sensitivity limits are taken into account. The bias-corrected frequency of binaries drops by a factor of 7.8 from  $q = 1$  to  $q = 0.5$ , even though most imaging programs are complete for companions down to or below this limit. A fit to the bias-corrected distribution for  $q > 0.5$  to a power-law,  $f(q) \propto q^\gamma$ , yields  $\gamma = 4.2 \pm 1.0$ , slightly flatter but nevertheless consistent with a Bayesian analysis of VLM binaries (Reid et al. 2006a).

In summary, our sample supports prior results on brown dwarf multiplicity, namely:

- The resolved binary fraction of brown dwarfs is lower than that of stars,  $\epsilon_b \approx 11\%$  for  $\rho \gtrsim 3$  AU and  $q \gtrsim 0.3$ ;
- The separation distribution of resolved brown dwarfs peaks around 4 AU; the true peak may lie at lower separations due to resolution limits of imaging programs;
- The maximum separations of field brown dwarf binaries appears to decrease for later spectral types, consistent with a mass-dependent trend; and

- Most brown dwarf pairs have near-equal mass ratios, with a bias-corrected distribution of  $f(q) \propto q^{(4.2 \pm 1.0)}$  indicated by current data.

These characteristics of brown dwarf field binaries provide key empirical constraints for the theoretical modeling of brown dwarf formation and dynamical evolution, issues that are discussed in detail in Burgasser et al. (2006b); Luhman et al. (2006); and Whitworth et al. (2006).

## 7. BINARIES AND THE L/T TRANSITION

### 7.1. *J*-band Brightening - Intrinsic to the L/T Transition

Three of the binaries in our sample – 2MASS 0518-2828, SDSS 0423-0414 and SDSS 1021-0304 – are composed of brown dwarfs that span the transition between L dwarfs and T dwarfs. This spectral type range has been the focus of both observational and theoretical studies as it encompasses dramatic changes in the atmospheric properties (e.g., photospheric condensate dust depletion) and spectral energy distributions (e.g., the onset of CH<sub>4</sub> absorption) of cool brown dwarfs. This transition also exhibits several unusual traits, including an apparent brightening of absolute *J*-band magnitudes from late-type L to mid-type T dwarfs (Dahn et al. 2002; Tinney, Burgasser & Kirkpatrick 2003; Vrba et al. 2004). This so-called “*J*-band bump” has been attributed to dynamic atmospheric processes, such as condensate cloud fragmentation (Burgasser et al. 2002b), a sudden increase in sedimentation efficiency (Knapp et al. 2004) or a global collapse of the condensate cloud layer (Tsuji 2005). However, Tsuji & Nakajima (2003) have also argued that age and/or surface gravity effects amongst disparate field sources may be responsible.

The component fluxes of the SDSS 1021-0304 binary demonstrate that the last hypothesis can be largely ruled out for this system. Under the reasonable assumption of coevality, these brown dwarfs have similar ages, masses and (presumably) radii, implying nearly identical surface gravities. Yet the T5 secondary of this system is clearly brighter than the T1 primary at 1.05 and 1.27  $\mu\text{m}$ . Similar trends suggested in the 2MASS 0518-2828 system and observed in SDSS 1534+1615 demonstrate that SDSS 1021-0304 is not a unique case. Hence, a brightening of surface fluxes at these wavelengths appears to be an *intrinsic feature* of the L/T transition.

### 7.2. A “Bump” or a “Plateau”?

In their analysis of the SDSS 1534+1615 binary, Liu et al. (2006) proposed that the *J*-band bump may be artificially enhanced by a significant contribution of binaries amongst mid-type T dwarfs (such “cryptobinarity” has also been suggested by Burrows, Sudarsky & Hubeny 2006). To examine this hypothesis in detail, Figure 16 compares absolute MKO *J*- and *K*-band magnitudes to spectral type for 50 L and T dwarf systems with measured parallaxes (Dahn et al. 2002; Tinney, Burgasser & Kirkpatrick 2003; Vrba et al. 2004, precision >20%), companions to nearby Hipparcos stars (Becklin & Zuckerman 1988; Nakajima et al. 1995; Burgasser et al. 2000b; Kirkpatrick et al. 2001; McCaughrean et al. 2004) and resolved absolute magnitudes for SDSS 0423-0414, SDSS 1021-0304 and the T1

+ T6 binary Epsilon Indi B (McCaughrean et al. 2004). For consistency, spectral types for L dwarfs are based on optical data and the Kirkpatrick et al. (1999) classification scheme, while those for T dwarfs are based on near infrared data and the Burgasser et al. (2006a) scheme. MKO *J* magnitudes for the SDSS 0423-0414 and SDSS 1021-0304 components are based on their F110W-F170M colors and Eqn. 2; *K*-band component photometry is derived from synthetic colors measured from the component spectral templates.

The *J*-band bump is seen clearly in these data in the T1-T5 spectral type range, and is well traced by the absolute magnitude/spectral type relation of Tinney, Burgasser & Kirkpatrick (2003). Yet one of these data points is the unresolved SDSS 1021-0304 systems, and its individual component fluxes are only slightly brighter ( $J = 14.33$  and  $14.29$ ) than the latest-type L dwarfs ( $J \sim 14.7$ ). The same holds true for the T2 secondary of SDSS 0423-0414 ( $J = 14.38$ ) and the T1 primary of Epsilon Indi B ( $J = 14.30$ ). Indeed, *all* of the resolved components spanning types T1 to T5, have nearly identical absolute *J*-band magnitudes.

Does this mean that the *J*-band bump is largely an artifact of multiplicity? Possibly, but only if the T2 SDSS 1254-0122, the T3.5 SDSS 1750+1759 (both unresolved in this study) and the T4.5 2MASS J05591914-1404488 (Burgasser et al. 2000c, unresolved in Burgasser et al. (2003c)) are all closely-separated multiples. This is not out of the realm of possibility, for as discussed in §6.2 the separations of brown dwarf binaries likely extend below imaging resolution limits. One or all of these systems may also have been imaged at an unfortunate orbital angle, as was the case initially for Kelu 1 (Martín, Brandner & Basri 1999; Liu & Leggett 2005; Gelino, Kulkarni & Stephens 2006). Furthermore, the fact that SDSS 1254-0122 and 2MASS 0559-1404 are  $\sim 0.5$  and  $\sim 0.8$  mag brighter at *J*-band than the T2 and T5 secondaries of SDSS 0423-0414 and SDSS 1021-0304, respectively, suggests that the former are unresolved multiples. If the primaries of these hypothetical systems are constrained to have  $M_J \approx 14.3$ , then the secondaries of SDSS 1254-0122 and SDSS 1750+1759 would have  $M_J \approx 15.3$ - $15.5$  and be  $\sim$ T6 dwarfs. 2MASS 0559-1404 would be required to have near equal-magnitudes components or be a higher multiple system. High resolution radial velocity monitoring observations are needed to test these possibilities.

It is important to point out that the absolute *J*-band magnitudes of the early-type T dwarf resolved binary components examined here are still  $\sim 0.4$  mag brighter than the latest-type L dwarfs (but  $\sim 0.5$  mag fainter at *K*-band). Hence, some broad-band brightening may still be present across the L/T transition. Furthermore, even if the *J*-band “bump” is a more modest “plateau”, there remains a significant ( $\sim 30\%$ ) brightening at 1.05 and 1.27  $\mu\text{m}$  due to flux redistribution within the *J*-band spectral region, a feature not yet reproduced self-consistently by current atmosphere models.

### 7.3. The Origin of *J*-band Brightening

That the observed brightening is concentrated in the 1.05 and 1.27  $\mu\text{m}$  flux peaks is an important clue to its origin. The photospheric atomic and molecular gas opacities of low-temperature brown dwarfs show distinct

minima at these wavelengths, shaped by strong H<sub>2</sub>O and CH<sub>4</sub> bands and bracketed by pressure-broadened K I at shorter wavelengths and collision-induced H<sub>2</sub> absorption at longer wavelengths. Condensate opacities, for grain sizes ( $\sim 40\text{--}80\ \mu\text{m}$ ) computed in a self-consistent manner (Ackerman & Marley 2001), are roughly constant across the near infrared band. In the L dwarf regime, condensates are a dominant source of opacity at the *J*-, *H*- and *K*-band spectral peaks. However, theoretical atmosphere models incorporating condensate clouds indicate that the photospheric opacity from these species are dominant only in the 1.05 and 1.27  $\mu\text{m}$  flux peaks for  $T_{\text{eff}} \lesssim 1300\text{--}1500\ \text{K}$ ; i.e., at the L/T transition (cf. Figure 16 in Burrows, Sudarsky & Hubeny 2006). If these condensates are suddenly removed, the total opacity at these wavelengths decreases, allowing brighter emission from deeper and hotter layers.

This is the underlying thesis for dynamical atmospheric explanations for the *J*-band brightening (Burgasser et al. 2002b; Knapp et al. 2004). However, one must also consider whether higher gas opacities at longer wavelengths, with the increased photospheric abundances of H<sub>2</sub>O and CH<sub>4</sub> molecules below  $T_{\text{eff}} \approx 1300\text{--}1800\ \text{K}$  (Burrows & Sharp 1999; Lodders & Fegley 2002) and stronger H<sub>2</sub> absorption, might lead to a redistribution of flux into the 1.05 and 1.27  $\mu\text{m}$  flux peaks. Current cloud models that assume constant sedimentation efficiency (Marley et al. 2002) or particle size distributions (Burrows, Sudarsky & Hubeny 2006) do not show this to be the case. Hence, a dynamic mechanism for clearing out photospheric condensate dust may still be necessary to explain the evolution of brown dwarf atmospheres across the L/T transition.

#### 7.4. The Frequency of L/T Binaries

Is there evidence from the distribution of binary frequency as a function of spectral type that binaries play a special role through the L/T transition? To address this, we have compiled results from high resolution imaging of L and T dwarfs by Koerner et al. (1999); Martín et al. (1999); Reid et al. (2001, 2006a); Close et al. (2003); Bouy et al. (2003); Burgasser et al. (2003c); Gizis et al. (2003); and this study.<sup>18</sup> We did not include individual binary discoveries made serendipitously (Goto et al. 2002; Potter et al. 2002; McCaughrean et al. 2004; Burgasser et al. 2005a) or those identified as part of as yet unpublished surveys (Liu et al. 2006; Stumpf, Bradner & Henning 2006) in order to make a fair assessment of the observed binary fraction. Care was taken to identify duplicate sources in each of the imaging studies, and classifications were verified through published optical (L dwarfs, on the Kirkpatrick et al. (1999) scheme) and near infrared data (T dwarfs, on the Burgasser et al. (2006a) scheme). Only those resolved pairs that had a high probability of companionship, based on either common proper motion confirmation, resolved spectroscopy and/or photometric colors, or very low probability of coincidence with an unrelated background source, were considered as bona-fide binaries. The complete sample includes 129 L dwarfs and

34 T dwarfs, of which 33 are binary.

Figure 17 plots the observed binary fraction of these sources as a function of spectral type, binned by individual subclasses and into subclass groups of L0-L2 (62 sources), L2.5-L4.5 (28 sources), L5-L6.5 (27 sources), L7-L9.5 (12 sources), T0-T3.5 (7 sources), T4-T5.5 (12 sources) and T6-T8 (15 sources). Note that these fractions have not been corrected for selection bias (resulting in an overestimate from equal-brightness systems) or sensitivity/resolution limits (resulting in an underestimate by missing closely separated or low mass ratio systems). This sample may also be subject to more subtle biases, such as the smaller typical distances of later-type, intrinsically fainter brown dwarfs, resulting in greater linear resolution for these objects (although this effect may be offset by the apparent decrease in separations for lower-mass brown dwarfs). It nevertheless serves to illustrate possible trends.

There is clearly significant structure in the binary fraction distribution for individual subclasses, although this could be attributed to small number statistics. By binning the subclasses (reducing statistical uncertainties), a remarkable result emerges. For most of the sample, binary fractions are consistent with the overall fraction,  $\epsilon_b^{\text{obs}} = 20 \pm 4\%$ . Yet the L7-L9.5 and T0-T3.5 subclass groups – the L/T transition objects — have fractions that are twice as high,  $42^{+12}_{-10}\%$  combining all 19 systems in this spectral type range. This deviation is significant at the 98% confidence level compared to the sample mean.

Why would the observed binary fraction of L/T transition objects be so high? We posit the following scenario. Analysis of the SDSS 0423-0414 and SDSS 1021-0304 components, and prior results from Kirkpatrick et al. (2000); Burgasser et al. (2002c); Dahn et al. (2002); Vrba et al. (2004) and Golimowski et al. (2004), all indicate that the L/T transition spans a relatively narrow range of effective temperatures,  $\Delta T_{\text{eff}} \approx 200\text{--}300\ \text{K}$ . However, the cooling rate of brown dwarfs is largely insensitive to changes in the photospheric opacity (Chabrier et al. 2000), such as the removal of condensates or emergence of CH<sub>4</sub> absorption. Brown dwarfs must therefore progress through the L/T transition relatively rapidly, implying fewer such sources per spectral subtype for a given field sample. On the other hand, the analysis of §5.3, and similar results by Cruz et al. (2004); Burgasser et al. (2005b); Reid et al. (2006b); and Liu et al. (2006), all demonstrate that early-type T dwarf spectral features can be reproduced from the combined light of a late-type L and mid-type T dwarf binary. It is therefore possible that such hybrid binaries, if unrecognized, could significantly contaminate a spectral sample of early-type T dwarfs.

To illustrate this point, consider the following example. Assuming that L5-L8 dwarfs have  $T_{\text{eff}} \approx 1700\text{--}1300\ \text{K}$  and L8-T5 dwarfs have  $T_{\text{eff}} \approx 1300\text{--}1100\ \text{K}$  (Table 5 and Golimowski et al. (2004)), the mass function simulations of Burgasser (2004) predict a relative space density of  $N_{L/T}/N_L \approx 0.9$  between these two groups, largely independent of the shape of the underlying mass function. However, because mid- to late-type L dwarfs are roughly twice as bright as L/T transition objects, the relative number observed in a magnitude-limited sample (the best approximation for current imaging samples) is

<sup>18</sup> We also include the recently identified Kelu 1 binary (Liu & Leggett 2005; Gelino, Kulkarni & Stephens 2006), a target of prior searches.

$(N_{L/T}/N_L)^{obs} \approx 0.3$ . Now consider that all brown dwarfs in a magnitude-limited sample have a resolvable binary fraction of  $\sim 25\%$ , and that 20% of all late-type L dwarf binaries have T dwarf secondaries (this is roughly consistent with the mass ratio distribution of Figure 15). These binaries would exhibit a combined light spectrum similar to a late-type L/early-type T dwarf, and would be identified as such in an unresolved spectroscopic sample. Hence, the observed binary fraction among late-type L dwarfs in this scenario would be  $\sim 20\%$ , while the fraction of L/T transition binaries would be

$$\epsilon_{L/T}^{obs} = \frac{0.2 \times 0.25 N_L + 0.25 N_{L/T}}{0.2 \times 0.25 N_L + N_{L/T}} = \frac{0.05 + 0.075}{0.05 + 0.3} \approx 36\%; \quad (9)$$

i.e., nearly twice the underlying binary fraction. This numerical example serves to illustrate that the binary hypothesis provides both a qualitative and quantitative explanation for the peak in the binary fraction of L/T transition objects. More complete modeling of this effect will be presented in a forthcoming publication.

We therefore conclude that multiplicity does play an important role in the L/T transition, contaminating samples of “true” transition objects and leading to a greater  $J$ -band brightening than that inferred for resolved systems. These binaries also provide a detailed and intriguing picture of this still poorly-understood transition, and a list of all currently known L/T binaries is given in Table 7. Further study of these source will provide improved understanding of the physical mechanisms governing this transition, including the depletion of photospheric condensates, the emergence of  $\text{CH}_4$  gas and the possible role of atmospheric dynamics in brown dwarf spectral evolution.

## 8. SUMMARY

We have identified 5 binaries in of a sample of 22 T dwarfs imaged with *HST* NICMOS. Of these, three are well-resolved, permitting determination of their component spectral types, relative bolometric luminosities and  $T_{eff}$ s, and systemic mass ratios. The identification of 2MASS 0518-2828 as a closely-separated binary confirms previous suspicions of multiplicity based on this object’s unusual near infrared spectrum. The bias-corrected resolved binary fraction of this sample ( $\epsilon_b = 11_{-3}^{+7}\%$ ), the near-unity mass ratios of the components of these systems ( $q \gtrsim 0.7$ ) and their small projected separations ( $\rho \lesssim 5$  AU) are all consistent with previously identified trends amongst VLM dwarfs, indicating that they are salient properties of brown dwarf field binaries.

Three of the binaries in our sample, SDSS 0423-0414, 2MASS 0518-2828 and SDSS 1021-0304, are composed of sources spanning the L to T transition, and spectral decomposition analysis of SDSS 1021-0304 reveals that its T5 secondary is 25–30% brighter at 1.05 and 1.27  $\mu\text{m}$  than its T1 primary, despite being 35% less luminous overall. The properties of these sources, as well as the recently discovered binary SDSS 1534+1615, indicate that the  $J$ -band brightening previously observed amongst late-type L and mid-type field T dwarfs is an intrinsic feature of the L/T transition and not the result of age, surface gravity or metallicity effects. In support of the results of Burrows, Sudarsky & Hubeny (2006) and Liu et al. (2006), we find that the  $J$ -band bump may be

more of a  $J$ -band “plateau”, with T1-T5 dwarfs having  $M_J \approx 14.3$ , enhanced by the presence of unresolved binaries in this spectral type range. Indeed, we find that the frequency of L/T transition binaries is twice as high as those of all other L and T dwarfs, a statistically significant deviation that can be explained if spectroscopic samples of L/T transition objects are significantly contaminated by binaries composed of earlier-type and later-type components. Taken together, the properties of L/T binary systems provide the most conclusive evidence to date that the L/T transition occurs relatively rapidly, driven by the removal of photospheric condensates that is likely to be facilitated by dynamic atmospheric processes. Further parallax and multiplicity measurements will better constrain the flux evolution and relative numbers of L/T transition objects, important constraints for understanding the physical mechanism of photospheric condensate depletion and the atmospheric evolution of brown dwarfs as they cool below  $T_{eff} \approx 1500$  K.

The authors would like to thank Santiago Arribas and Patricia Royle at STScI for their technical support of *HST* program GO-9833, and David Sprayberry and Meg Whittle at Keck for their support during the NIRC observations of 2MASS 1553+1532. A. J. B. acknowledges useful discussions with Antonin Bouchez, Randy Campbell, Michael Liu (who gave our original manuscript a careful read), Mark McCaughrean and Frederick Vrba. We also thank our referee, Brian Patten, for his prompt critique of our manuscript and helpful suggestions. K. L. C. acknowledges support by a National Science Foundation Astronomy and Astrophysics Postdoctoral Fellowship under AST-0401418. A. B. acknowledges support under NASA grant NNG04GL22G and through the NASA Astrobiology Institute under Cooperative Agreement No. CAN-02-OSS-02 issued through the Office of Space Science. This work is based in part on observations made with the NASA/ESA Hubble Space Telescope, obtained at the Space Telescope Science Institute, which is operated by the Association of Universities for Research in Astronomy, Inc., under NASA contract NAS 5-26555. These observations are associated with proposals GO-9833 and GO-10247. This publication makes use of data from the Two Micron All Sky Survey, which is a joint project of the University of Massachusetts and the Infrared Processing and Analysis Center, and funded by the National Aeronautics and Space Administration and the National Science Foundation. 2MASS data were obtained from the NASA/IPAC Infrared Science Archive, which is operated by the Jet Propulsion Laboratory, California Institute of Technology, under contract with the National Aeronautics and Space Administration. This publication has benefitted from the M, L, and T dwarf compendium housed at DwarfArchives.org and maintained by Chris Gelino, Davy Kirkpatrick, and Adam Burgasser; and the VLM Binary Archive maintained by N. Sieglar at [http://paperclip.as.arizona.edu/\\$\sim\\$nsieglar/VLM\\_binar](http://paperclip.as.arizona.edu/$\sim$nsieglar/VLM_binar). The authors wish to recognize and acknowledge the very significant cultural role and reverence that the summit of Mauna Kea has always had within the indigenous Hawaiian community. We are most fortunate to have the opportunity to conduct observations from this

mountain.

Facilities: Hubble Space Telescope(NICMOS);

IRTF(SpeX); Keck(NIRC)

#### REFERENCES

- Abt, H. A., & Levy, S. G. 1976, *ApJS*, 30, 273
- Ackerman, A. S., & Marley, M. S. 2001, *ApJ*, 556, 872
- Allard, F., Hauschildt, P. H., Alexander, D. R., Tamanai, A., & Schweitzer, A. 2001, *ApJ*, 556, 357
- Allard, N. F., Allard, F., Hauschildt, P. H., Kielkopf, J. F., & Machin, L. 2003, *A&A*, 411, L473
- An, J. H., et al. 2002, *ApJ*, 572, 521
- Basri, G., & Martín, E. L. 1999, *AJ*, 118, 2460
- Bate, M. R., Bonnell, I. A., & Bromm, V. 2002, *MNRAS*, 332, L65
- Becklin, E. E., & Zuckerman, B. 1988, *Nature*, 336, 656
- Billeres, M., Delfosse, X., Beuzit, J.-L., Forveille, T., Marchal, L., & Martín, E. L. 2005, *A&A*, 440, L55
- Brandner, W., Marin, E. L., Bouy, H., Köhler, R., Delfosse X., Basri, G., & Andersen, M. 2004, *A&A*, 428, 205
- Bouy, H., Moraux, E., Bouvier, J., Brandner, W., Martín, E. L., Allard, F., Baraffe, I., & Fernández, M. 2006, *AJ*, 637, 1056
- Bouy, H., Brandner, W., Martín, E. L., Delfosse, X., Allard, F., & Basri, G. 2003, *AJ*, 126, 1526
- Bouy, H., Martín, E. L., Brandner, W., & Bouvier, J. 2005, *AJ*, 129, 511
- Bouy, H., et al. *A&A*, 2004, 423, 341
- Burgasser, A. J., Geballe, T. R., Leggett, S. K., Kirkpatrick, J. D., & Golimowski, D. A. 2006a, *ApJ*, 637, 1067
- Burgasser, A. J., Kirkpatrick, J. D., & Brown, M. E. 2002, *BAAS*, 200, 1105
- Burgasser, A. J., Kirkpatrick, J. D., Liebert, J., & Burrows, A. 2003a, *ApJ*, 594, 510
- Burgasser, A. J. 2004, *ApJS*, 155, 191
- Burgasser, A. J., Kirkpatrick, J. D., & Lowrance, P. J. 2005a, *AJ*, 129, 2849
- Burgasser, A. J., Kirkpatrick, J. D., McElwain, M. W., Cutri, R. M., Burgasser, A. J., & Skrutskie, M. F. 2003b, *AJ*, 125, 850
- Burgasser, A. J., Kirkpatrick, J. D., Reid, I. N., Brown, M. E., Miskey, C. L., & Gizis, J. E. 2003c, *ApJ*, 586, 512
- Burgasser, A. J., Kirkpatrick, J. D., Reid, I. N., Liebert, J., Gizis, J. E., & Brown, M. E. 2000a, *AJ*, 120, 473
- Burgasser, A. J., Liebert, J., Kirkpatrick, J. D., & Gizis, J. E. 2002a, *AJ*, 123, 2744
- Burgasser, A. J., Marley, M. S., Ackerman, A. S., Saumon, D., Ladders, K., Dahn, C. C., Harris, H. C., & Kirkpatrick, J. D. 2002b, *ApJ*, 571, L151
- Burgasser, A. J., McElwain, M. W., & Kirkpatrick, J. D. 2003, *AJ*, 126, 2487
- Burgasser, A. J., McElwain, M. W., Kirkpatrick, J. D., Cruz, K. L., Tinney, C. G., & Reid, I. N. 2004a, *AJ*, 127, 2856
- Burgasser, A. J., Reid, I. N., Siegler, N., Close, L. M., Allen, P., Lowrance, P. J., & Gizis, J. E. 2006b, in *Planets and Protostars V*, eds. B. Reipurth, D. Jewitt and K. Keil (Univ. Arizona Press: Tucson), in press
- Burgasser, A. J., Reid, I. N., Leggett, S. J., Kirkpatrick, J. D., Liebert, J., & Burrows, A. 2005b, *ApJ*, 634, L177
- Burgasser, A. J., et al. 1999, *ApJ*, 522, L65
- . 2000b, *ApJ*, 531, L57
- . 2000c, *AJ*, 120, 1100
- . 2002c, *AJ*, 564, 421
- Burrows, A., et al. 1997, *ApJ*, 491, 856
- Burrows, A., Hubbard, W. B., Lunine, J. I., & Liebert, J. 2001, *Rev. of Modern Physics*, 73, 719
- Burrows, A., Marley, M. S., & Sharp, C. M. 2000, *ApJ*, 531, 438
- Burrows, A., & Sharp, C. M. 1999, *ApJ*, 512, 843
- Burrows, A., Sudarsky, D., & Hubeny, I. 2006, *ApJ*, 640, 1063
- Burrows, A., Sudarsky, D., & Lunine, J. I. 2003, *ApJ*, 596, 587
- Burrows, A., & Volobuyev, M. 2003, *ApJ*, 583, 985
- Bushouse, H., MacKenty, J., Skinner, C., & Stobie, E. 1997, in *ASP Conf. Ser. 125, Astronomical Data Analysis Software and Systems VI*, ed. G. Hunt & H. E. Payne (ASP: San Francisco), 439
- Chabrier, G., Baraffe, I., Allard, F., & Hauschildt, P. 2000, *ApJ*, 542, 464
- Chauvin, G., Lagrange, A.-M., Dumas, C., Zuckerman, B., Mouillet, D., Song, I., Beuzit, J.-L., & Lowrance, P. 2004, *A&A*, 425, L29
- . 2005, *A&A*, 438, L25
- Close, L. M., Siegler, N., Freed, M., & Biller, B. 2003, *ApJ*, 587, 407
- Cruz, K. L., Burgasser, A. J., Reid, I. N., & Liebert, J. *ApJ*, 2004, 604, L61
- Cruz, K. L., Reid, I. N., Liebert, J., Kirkpatrick, J. D., & Lowrance, P. J. 2003, *AJ*, 126, 2421
- Dahn, C. C., et al. 2002, *AJ*, 124, 1170
- Delfosse X., Beuzit J.-L., Marchal L., Bonfils X. C., Perrier, C., et al. 2004, in *Spectroscopically and Spatially Resolving the Components of the Close Binary Stars*, ed. R. W. Hilditch et al., (ASP: San Francisco), p. 166
- Delfosse, X., et al. 1997, *A&A*, 327, L25
- Duquenoey, A., & Mayor, M. 1991, *A&A*, 248, 485
- ESA, 1997, *The Hipparcos and Tycho Catalogues*, ESA SP-1200
- Fischer, D. A., & Marcy, G. W. 1991, *ApJ*, 396, 178
- Geballe, T. R., et al. 2002, *ApJ*, 564, 466
- Gelino, C. R., Kulkarni, S. R., & Stephens, D. C. 2006, *PASP*, 118, 611
- Gizis, J. E. 2002, *ApJ*, 575, 484
- Gizis, J. E., Monet, D. G., Reid, I. N., Kirkpatrick, J. D., Liebert, J., & Williams, R. 2000, *AJ*, 120, 1085
- Gizis, J. E., Reid, I. N., Knapp, G. R., Liebert, J., Kirkpatrick, J. D., Koerner, D. W., & Burgasser, A. J. 2003, *AJ*, 125, 3302
- Golimowski, D. A., et al. 2004, *AJ*, 127, 3516
- Goto, M., et al. 2002, 567, L59
- Hawley, S. L., Reid, I. N., Gizis, J. E., & Byrne, P. B. 1999, in *ASP Conf. Ser. 158, Solar and Stellar Activity: Similarities and Differences*, ed. C. J. Butler & J. G. Doyle (San Francisco: ASP), p. 63
- in *Solar and Stellar Activity: Similarities and Differences*, ASP Conf. Ser. 158, ed. C. J. Butler & J. G. Doyle (ASP), p.63
- Hayashi, C., & Nakano, T. 1963, *Prog. Theo. Physics*, 30, 4
- Joergens, V. 2006, *A&A*, 446, 1165
- Kirkpatrick, J. D., Dahn, C. C., Monet, D. G., Reid, I. N., Gizis, J. E., Liebert, J., & Burgasser, A. J. 2001, *AJ*, 121, 3235
- Kirkpatrick, J. D., Reid, I. N., Liebert, J., Gizis, J. E., Burgasser, A. J., Monet, D. G., Dahn, C. C., Nelson, B., & Williams, R. J. 2000, *AJ*, 120, 447
- Kirkpatrick, J. D., et al. 1999, *ApJ*, 519, 802
- Knapp, G., et al. 2004, *ApJ*, 127, 3553
- Koerner, D. W., Kirkpatrick, J. D., McElwain, M. W., & Bonaventura, N. R. 1999, *ApJ*, 526, L25
- Krist, H. 1995, in *ASP Conf. Ser. 77, Astronomical Data Analysis Software and Systems, IV*, ed. R. A. Shaw, H. E. Payne, & J. J. E. Hayes (San Francisco: ASP), 349
- Kumar, S. S. 1962, *AJ*, 67, 579
- Lane, B. F., Zapatero Osorio, M. R., Britton, M. C., Martín, E. L., & Kulkarni, S. R. 2001, *ApJ*, 560, 390
- Leggett, S. K., et al. 2000, *ApJ*, 536, L35
- Leggett, S. K., et al. 2002, *ApJ*, 564, 452
- Leinert, Ch., Jahreiβ, H., Woitas, J., Zucker, S., Mazeh, T., Eckart, A., & Köhler, R. 2001, *A&A*, 367, 183
- Liu, M. C., & Leggett, S. K. 2005, *ApJ*, 634, 616
- Liu, M. C., Leggett, S. K., Golimowski, D. A., Chiu, K., Fan, X., Geballe, T. R., Schneider, D. P., & Brinkmann, J. 2006, *ApJ*, in press
- Ladders, K. 1999, *ApJ*, 519, 793
- Ladders, K., & Fegley, B. 2002, *Icarus*, 155, 393
- Luhman, K. L. 2004, *ApJ*, 614, 398
- Luhman, K. L., Joergens, V., Lada, C., Muzerolle, J., Pascucci, I., & White, R. 2006, in *Planets and Protostars V*, eds. B. Reipurth, D. Jewitt and K. Keil (Univ. Arizona Press: Tucson), in press
- Marcy, G. W., & Butler, R. P. 2000, *PASP*, 112, 137
- Marley, M. S., Saumon, D., Guillot, T., Freedman, R. S., Hubbard, W. B., Burrows, A., & Lunine, J. I. 1996, *Science*, 272, 1919
- Marley, M. S., Seager, S., Saumon, D., Ladders, K., Ackerman, A. S., Freedman, R., & Fan, X. 2002, *ApJ*, 568, 335
- Martín, E. L., Brandner, W., & Basri, G. 1999, *Science*, 283, 1718
- Martín, E. L., Brandner, W., Bouvier, J., Luhman, K. L., Stauffer, J., Basri, G., Zapatero Osorio, M. R., & Barrado y Navascués, D. 2000, *ApJ*, 543, 299
- Martín, E. L., Delfosse, X., Basri, G., Goldman, B., Forveille, T., & Zapatero Osorio, M. R. 1999, *AJ*, 118, 2466

- Matthews, K., & Soifer, B. T. 1994, in *Infrared Astronomy with Arrays: The Next Generation*, ed. I. McLean (Dordrecht: Kluwer), 239
- Maxed, P. F. L., & Jeffries, R. D. 2005, *MNRAS*, 326, L45
- Mazeh, T., Goldberg, D., Duquenois, A., & Mayor, M. 1992, *ApJ*, 401, 265
- McCaughrean, M., Close, L. M., Scholz, R.-D., Lenzen, R., Biller, B., Brandner, W., Hartung, M., & Lodieu, N. 2004, *A&A*, 413, 1029
- Mohanty, S., & Basri, G. 2003, *ApJ*, 583, 451
- Mugrauer, M., & Neuhäuser, R. 2005, *AN*, 326, 701
- Nakajima, T., Oppenheimer, B. R., Kulkarni, S. R., Golimowski, D. A., Matthews, K., & Durrance, S. T. 1995, *Nature*, 378, 463
- Oppenheimer, B. R., Kulkarni, S. R., Matthews, K., & Nakajima, T. 1995, *Science*, 270, 1478
- Potter, D., Martín, E. L., Cushing, M. C., Baudoz, P., Brandner, W., Guyon, O., & Neuhäuser, R. 2002, *ApJ*, 567, L133
- Rayner, J. T., Toomey, D. W., Onaka, P. M., Denault, A. J., Stahlberger, W. E., Vacca, W. D., Cushing, M. C., & Wang, S. 2003, *PASP*, 155, 362
- Rebolo, R., Martín, E. L., & Magazzu, A. 1992, *ApJ*, 389, L83
- Rebolo, R., Zapatero Osorio, M. R., Madrugá, S., Béjar, V. J. S., Arribas, S., & Licandro, J. 1998, *Science*, 282, 1309
- Reid, N. 2003, *MNRAS*, 342, 837
- Reid, I. N., Gizis, J. E., Kirkpatrick, J. D., & Koerner, D. 2001, *AJ*, 121, 489
- Reid, I. N., & Gizis, J. E. 1997, *AJ*, 113, 2246
- Reid, I. N., & Hawley, S. L. 2000, *New Light on Dark Stars* (Chichester: Praxis)
- Reid, I. N., Lewitus, E., Allen, P., Cruz, K. L., & Burgasser, A. J. 2006a, *ApJ*, in press
- Reid, I. N., Lewitus, E., Cruz, K. L., & Burgasser, A. J. 2006b, *ApJ*, 639, 1114
- Ruiz, M. T., Leggett, S. K., & Allard, F. 1997, *ApJ*, 491, L107
- Schultz, A., et al. 2005, *NICMOS Instrument Handbook*, Version 8.0, (Baltimore: STScI).
- Skrutskie, M. F., et al. 2006, *AJ*, 131, 1163
- Siegler, N., Close, L. M., Cruz, K. L., Martín, E. L., & Reid, I. N. 2005, *ApJ*, 621, 1023
- Simons, D. A., & Tokunaga, A. T. 2002, *PASP*, 114, 169
- Skumanich, A. 1972, *ApJ*, 171, 565
- Stassun, K., Mathieu, R. D., Vaz, L. P. R., Valenti, J. A., & Gomez, Y. 2006, *Nature*, in press
- Strauss, M. A., et al. 1999, *ApJ*, 522, L61
- Stephens, D. C., & Leggett, S. K. 2004, *PASP*, 166, 9
- Stumpf, M. B., Brandner, W., & Henning, Th. 2006, in *Planets and Protostars V*, eds. B. Reipurth, D. Jewitt and K. Keil (Univ. Arizona Press: Tucson), in press
- Tinney, C. G., Burgasser, A. J., & Kirkpatrick, J. D. 2003, *AJ*, 126, 975
- Tinney, C. G., Burgasser, A. J., Kirkpatrick, J. D., & McElwain, M. W. 2005, *AJ*, 130, 2326
- Tokunaga, A. T., Simons, D. A., & Vacca, W. D. 2002, *PASP*, 114, 180
- Tsuji, T. 2005, *ApJ*, 621, 1033
- Tsuji, T., & Nakajima, T. 2003, *ApJ*, 585, L151
- Tsuji, T., Ohnaka, K., Aoki, W., & Nakajima, T. 1996, *A&A*, 308, L29
- Vrba, F. J., et al. 2004, *AJ*, 127, 2948
- West, A. A., et al. 2004, *AJ*, 128, 426
- Whitworth, A., Bate, M. R., Nordlund, A., Reipurth, B., & Zinnecker, H. 2006, in *Planets and Protostars V*, eds. B. Reipurth, D. Jewitt and K. Keil (Univ. Arizona Press: Tucson), in press
- York, D. G., et al. 2000, *AJ*, 120, 1579
- Zapatero Osorio, M. R., Lane, B. F., Pavlenko, Ya., Martín, E. L., Britton, M., & Kulkarni, S. R. 2004, *ApJ*, 615, 958

TABLE 1  
T DWARF TARGETS

Name	SpT <sup>a</sup>	J2000 Coordinates <sup>b</sup>			2MASS Photometry			$\pi$ (arcs)	$\mu$ (arcs)
		$\alpha$	$\delta$	Epoch	$J$ (mag)	$H$ (mag)	$K_s$ (mag)		
(1)	(2)	(3)	(4)	(5)	(6)	(7)	(8)	(9)	(10)
SDSS J015141.69+124429.6	T1	01 <sup>h</sup> 51 <sup>m</sup> 41 <sup>s</sup> .55	+12°44′30″.0	1997.70	16.57±0.13	15.60±0.11	15.18±0.19	0.047±0.003	0.743±0.010
SDSS J020742.48+000056.2	T4.5	02 <sup>h</sup> 07 <sup>m</sup> 42 <sup>s</sup> .84	+00°00′56″.4	2000.63	16.63±0.05 <sup>d</sup>	16.66±0.05 <sup>d</sup>	16.62±0.05 <sup>d</sup>	0.035±0.010	0.156±0.010
2MASS J02431371-2453298	T6	02 <sup>h</sup> 43 <sup>m</sup> 13 <sup>s</sup> .71	-24°53′29″.8	1998.87	15.38±0.05	15.14±0.11	15.22±0.17	0.094±0.004	0.355±0.010
2MASS J03480772-6022270	T7	03 <sup>h</sup> 48 <sup>m</sup> 07 <sup>s</sup> .72	-60°22′27″.0	1999.89	15.32±0.05	15.56±0.14	15.60±0.23	...	0.77±0.010
2MASS J04151954-0935066	T8	04 <sup>h</sup> 15 <sup>m</sup> 19 <sup>s</sup> .54	-09°35′06″.6	1998.87	15.70±0.06	15.54±0.11	15.43±0.20	0.174±0.003	2.255±0.010
SDSS J042348.57-041403.5	T0	04 <sup>h</sup> 23 <sup>m</sup> 48 <sup>s</sup> .58	-04°14′03″.5	1998.73	14.47±0.03	13.46±0.04	12.93±0.03	0.0659±0.0017	0.333±0.010
2MASS J05160945-0445499	T5.5	05 <sup>h</sup> 16 <sup>m</sup> 09 <sup>s</sup> .45	-04°45′49″.9	1998.72	15.98±0.08	15.72±0.17	15.49±0.20	...	0.34±0.010
2MASS J05185995-2828372	T1p	05 <sup>h</sup> 18 <sup>m</sup> 59 <sup>s</sup> .95	-28°28′37″.2	1999.01	15.98±0.10	14.83±0.07	14.16±0.07	...	...
2MASS J07271824+1710012	T7	07 <sup>h</sup> 27 <sup>m</sup> 18 <sup>s</sup> .24	+17°10′01″.2	1997.83	15.60±0.06	15.76±0.17	15.56±0.19	0.110±0.002	1.297±0.010
2MASS J07554795+2212169	T5	07 <sup>h</sup> 55 <sup>m</sup> 47 <sup>s</sup> .95	+22°12′16″.9	1998.83	15.73±0.06	15.67±0.15	15.75±0.21	...	...
SDSS J083717.22-000018.3	T1	08 <sup>h</sup> 37 <sup>m</sup> 17 <sup>s</sup> .21	-00°00′18″.0	2000.11	16.90±0.05 <sup>d</sup>	16.21±0.05 <sup>d</sup>	15.98±0.05 <sup>d</sup>	0.034±0.014	0.173±0.010
SDSS J092615.38+584720.9	T4.5	09 <sup>h</sup> 26 <sup>m</sup> 15 <sup>s</sup> .37	+58°47′21″.2	2000.22	15.90±0.07	15.31±0.10	15.45±0.19	...	< 0.010
SDSS J102109.69-030420.1	T3	10 <sup>h</sup> 21 <sup>m</sup> 09 <sup>s</sup> .69	-03°04′19″.7	1998.94	16.25±0.09	15.35±0.10	15.13±0.17	0.034±0.005	0.183±0.010
SDSS J111010.01+011613.1	T5.5	11 <sup>h</sup> 10 <sup>m</sup> 10 <sup>s</sup> .01	+01°16′13″.0	2000.12	16.34±0.12	15.92±0.14	> 15.1	...	0.34±0.010
2MASS J12171110-0311131	T7.5	12 <sup>h</sup> 17 <sup>m</sup> 11 <sup>s</sup> .10	-03°11′13″.1	1999.08	15.86±0.06	15.75±0.12	> 15.9	0.091±0.002	1.0571±0.010
SDSS J125453.90-012247.4	T2	12 <sup>h</sup> 54 <sup>m</sup> 53 <sup>s</sup> .93	-01°22′47″.4	1999.07	14.89±0.04	14.09±0.03	13.84±0.05	0.0732±0.0019	0.491±0.010
2MASS J15031961+2525196	T5	15 <sup>h</sup> 03 <sup>m</sup> 19 <sup>s</sup> .61	+25°25′19″.6	1999.39	13.94±0.02	13.86±0.03	13.96±0.06	...	...
2MASS J15530228+1532369	T7	15 <sup>h</sup> 53 <sup>m</sup> 02 <sup>s</sup> .28	+15°32′36″.9	1998.15	15.83±0.07	15.94±0.16	15.51±0.18	...	...
SDSS J162414.37+002915.6	T6	16 <sup>h</sup> 24 <sup>m</sup> 14 <sup>s</sup> .36	+00°29′15″.8	1999.31	15.49±0.05	15.52±0.10	> 15.5	0.092±0.002	0.3832±0.010
SDSS J175032.96+175903.9	T3.5	17 <sup>h</sup> 50 <sup>m</sup> 32 <sup>s</sup> .93	+17°59′04″.2	1999.23	16.34±0.10	15.95±0.13	15.48±0.19	0.036±0.005	0.204±0.010
2MASS J22282889-4310262	T6	22 <sup>h</sup> 28 <sup>m</sup> 28 <sup>s</sup> .89	-43°10′26″.2	1998.90	15.66±0.07	15.36±0.12	15.30±0.21	...	0.31±0.010
2MASS J22541892+3123498	T4	22 <sup>h</sup> 54 <sup>m</sup> 18 <sup>s</sup> .92	+31°23′49″.8	1998.48	15.26±0.05	15.02±0.08	14.90±0.15	...	...
2MASS J23391025+1352284	T5	23 <sup>h</sup> 39 <sup>m</sup> 10 <sup>s</sup> .25	+13°52′28″.4	2000.91	16.24±0.11	15.82±0.15	16.15±0.31	...	0.83±0.010

REFERENCES. — (1) Geballe et al. (2002); (2) Burgasser et al. (2002c); (3) Burgasser, McElwain & Kirkpatrick (2003); (4) Cruz et al. (2004); (5) Leggett et al. (1999); (6) Burgasser et al. (2003b); (7) Burgasser et al. (2003b); (8) Strauss et al. (1999); (9) Vrba et al. (2004); (10) Tinney, Burgasser & Kirkpatrick (2003); (11) Tinney, Burgasser & Kirkpatrick (2003); (12) Dahn et al. (2002).

<sup>a</sup>Near infrared spectral types from Burgasser et al. (2006a).

<sup>b</sup>Coordinates from the 2MASS All Sky Point Source Catalog (Skrutskie et al. 2006).

<sup>c</sup>Discovery reference in boldface type, followed by references for additional photometric and astrometric data.

<sup>d</sup>MKO *JHK* from Leggett et al. (2002) or Knapp et al. (2004).

TABLE 2  
LOG OF *HST* OBSERVATIONS FOR PROGRAMS GO-9833 AND GO-10247.

Object	UT Date	F090M		F110W		F170M		Roll Angle <sup>b</sup> (°)
		<i>t</i> (s)	<i>m<sub>lim</sub></i> <sup>a</sup> (mag)	<i>t</i> (s)	<i>m<sub>lim</sub></i> <sup>a</sup> (mag)	<i>t</i> (s)	<i>m<sub>lim</sub></i> <sup>a</sup> (mag)	
(1)	(2)	(3)	(4)	(5)	(6)	(7)	(8)	(9)
SDSS 0151+1244	2003 Nov 3	56	19.0	864	22.9	1519	21.2	212.0
SDSS 0207+0000	2004 Feb 3	48	18.4	864	22.1	1519	20.9	208.1
2MASS 0243–2453	2004 Feb 15	56	19.5	864	23.6	1519	21.5	220.6
2MASS 0348–6022	2004 May 26	88	20.2	1599	22.7	3071	21.4	321.1
2MASS 0415–0935	2004 Feb 20	56	19.0	864	22.6	1519	21.1	214.1
SDSS 0423–0414	2004 Jul 22	72	19.3	816	22.6	1519	21.3	15.3
2MASS 0516–0445	2004 Jul 25	48	18.6	864	22.7	1519	21.1	15.9
2MASS 0518–2828 <sup>c</sup>	2004 Sep 7	960	21.0	64	19.9	416	19.9	38.9
2MASS 0727+1710	2004 Mar 27	56	19.5	864	23.6	1519	21.1	232.7
2MASS 0755+2212	2004 Mar 29	56	18.6	864	22.4	1519	20.9	236.9
SDSS 0837–0000	2004 Feb 18	48	18.6	864	23.3	1519	21.7	196.5
SDSS 0926+5847	2004 Feb 5	48	19.1	960	22.7	1600	21.2	319.5
SDSS 1021–0304	2004 May 22	48	18.9	864	22.9	1519	21.0	245.9
SDSS 1110+0116	2004 May 22	48	18.9	864	23.3	1519	21.5	247.1
2MASS 1217–0311	2004 Apr 26	48	18.7	864	22.7	1519	21.3	255.7
SDSS 1254–0122	2004 Feb 13	...	...	896	22.7	1519	21.1	64.9
2MASS 1503+2525	2003 Sep 9	80	18.9	791	21.9	1519	20.7	216.0
2MASS 1553+1532	2003 Sep 7	56	19.5	864	23.5	1519	21.7	226.9
SDSS 1624+0029	2003 Sep 9	48	18.8	864	22.7	1519	20.9	230.8
SDSS 1750+1759	2003 Sep 12	56	18.6	864	22.1	1519	20.9	231.8
2MASS 2228–4310	2004 May 26	72	19.2	912	23.0	1519	21.3	37.3
2MASS 2254+3123	2003 Sep 15	64	19.4	864	22.8	1519	21.2	299.7
2MASS 2339+1352	2003 Nov 1	56	18.8	864	22.6	1519	20.9	218.5

<sup>a</sup>Limiting magnitude estimated for a  $5\sigma$  flux peak detection.

<sup>b</sup>Telescope roll angle, East from North.

<sup>c</sup>Also observed at F145M (320 s) and F160W (160 s).

TABLE 3  
NICMOS NIC1 APERTURE CORRECTIONS.

Aperture Radius (pixels)	F090M <sup>a</sup> (mag)	F110W (mag)	F170M (mag)
2.0	-0.71±0.05	-0.79±0.02	-1.096±0.009
2.5	-0.60±0.04	-0.695±0.017	-0.869±0.012
3.0	-0.47±0.04	-0.637±0.014	-0.757±0.008
3.5	-0.35±0.04	-0.557±0.011	-0.714±0.008
4.0	-0.26±0.04	-0.451±0.008	-0.694±0.007
4.5	-0.22±0.04	-0.349±0.007	-0.658±0.007
5.0 <sup>b</sup>	-0.20±0.05	-0.275±0.005	-0.593±0.006
5.5	-0.18±0.05	-0.232±0.005	-0.503±0.006
6.0	-0.17±0.04	-0.211±0.004	-0.410±0.006
6.5	-0.16±0.04	-0.199±0.003	-0.333±0.006
7.0	-0.15±0.03	-0.190±0.003	-0.279±0.005
7.5	-0.14±0.03	-0.181±0.002	-0.247±0.004
8.0	-0.14±0.03	-0.1736±0.0019	-0.232±0.004
8.5	-0.14±0.04	-0.1681±0.0015	-0.225±0.004
9.0	-0.13±0.04	-0.1638±0.0012	-0.219±0.003
9.5	-0.12±0.04	-0.1597±0.0010	-0.212±0.002
10.0	-0.12±0.04	-0.1549±0.0007	-0.2039±0.0017
10.5	-0.11±0.02	-0.1498±0.0006	-0.1969±0.0013
11.0	-0.115±0.012	-0.1448±0.0006	-0.1919±0.0009

NOTE. — Values include corrections from a reference aperture (11.5 pixels) to an infinitely sized aperture of -0.1136, -0.1393 and -0.1888 mag as given in Schultz et al. (2005).

<sup>a</sup>Measured from observations of 2MASS 0518-2828.

<sup>b</sup>Adopted aperture radius for single sources.

TABLE 4  
NICMOS PHOTOMETRY.

Object	SpT	F090M (mag)	F110W (mag)	F170M (mag)	F110W-F170M (mag)
(1)	(2)	(3)	(4)	(5)	(6)
SDSS 0151+1244	T1	18.53±0.09	17.26±0.05	15.54±0.05	1.72±0.04
SDSS 0207+0000	T4.5	19.9±0.2	17.84±0.05	16.87±0.05	0.97±0.04
2MASS 0243–2453	T6	19.5±0.2	16.23±0.05	15.74±0.06	0.49±0.04
2MASS 0348–6022	T7	18.51±0.09	16.11±0.06	16.16±0.05	-0.05±0.05
2MASS 0415–0935	T8	19.04±0.10	16.47±0.05	16.67±0.06	-0.20±0.04
SDSS 0423–0414	T0	16.68±0.10 <sup>a</sup>	15.28±0.05 <sup>a</sup>	13.62±0.05 <sup>a</sup>	1.66±0.04 <sup>a</sup>
2MASS 0516–0445	T5.5	18.96±0.09	16.66±0.05	16.14±0.05	0.52±0.03
2MASS 0518–2828 <sup>b</sup>	T1p	18.55±0.08	16.69±0.07	14.92±0.05	1.77±0.06
2MASS 0755+2212	T5	18.89±0.09	16.58±0.05	16.08±0.05	0.50±0.03
SDSS 0837–0000	T1	>18.6	17.91±0.05	16.21±0.05	1.70±0.04
SDSS 0926+5847	T4.5	18.66±0.09	16.57±0.05	15.64±0.05	0.93±0.03
SDSS 1021–0304	T3	19.34±0.15 <sup>a</sup>	17.09±0.05 <sup>a</sup>	15.83±0.05 <sup>a</sup>	1.26±0.04 <sup>a</sup>
SDSS 1110+0116	T5.5	19.15±0.12	17.27±0.05	16.49±0.05	0.78±0.04
2MASS 1217–0311	T7.5	18.91±0.09	16.73±0.05	16.77±0.05	-0.04±0.04
SDSS 1254–0122	T2	...	15.66±0.05	14.10±0.05	1.56±0.03
2MASS 1503+2525	T5	16.84±0.08	14.65±0.05	14.18±0.05	0.47±0.03
2MASS 1553+1532A	T7	19.16±0.16	17.16±0.05	17.01±0.05	0.15±0.04
2MASS 1553+1532B	T7:	>19.5	17.46±0.05	17.40±0.05	0.06±0.04
SDSS 1624+0029	T6	18.46±0.09	16.28±0.05	15.96±0.05	0.32±0.03
SDSS 1750+1759	T3.5	18.80±0.09	17.18±0.05	16.04±0.05	1.14±0.04
2MASS 2228–4310	T6	18.77±0.09	16.36±0.05	16.05±0.05	0.31±0.03
2MASS 2254+3123	T4	18.12±0.10	16.05±0.05	15.09±0.05	0.96±0.04
2MASS 2339+1352	T5	18.86±0.09	16.91±0.05	16.27±0.05	0.64±0.03

NOTE. — Aperture photometry derived using an 5-pixel aperture and aperture corrections from Table 2, unless otherwise noted. Values are given on the Arizona Vega system ( $M_{Vega} = 0.02$ ). Uncertainties include RMS scatter in count rates between individual exposures, aperture correction uncertainties, 5% flux calibration (3% in F110W-F170M color) and 1% sensitivity variation (zeropoint drift).

<sup>a</sup>Photometry measured using a 15-pixel aperture and no aperture correction to incorporate both components.

<sup>b</sup>Additional photometry for 2MASS 0518-2828: F145M = 15.86±0.05, F160W = 15.20±0.05.

TABLE 5  
BINARY PROPERTIES.

Parameter	SDSS 0423-0414	2MASS 0518-2828	SDSS 0926+5847	SDSS 1021-0304	2MASS 1553+1532	
UT Date	2004 Jul 22	2004 Sep 7	2004 Feb 5	2004 May 22	2003 Sep 7	2000 Jul 22
Instrument	<i>HST</i> NICMOS	<i>HST</i> NICMOS	<i>HST</i> NICMOS	<i>HST</i> NICMOS	<i>HST</i> NICMOS	Keck NIRC
$\rho$ (")	0'164±0'005	0'051±0'012	0'070±0'006	0'172±0'005	0'349±0'005	0'30±0'02
(AU)	2.49±0.07	1.8±0.5	2.6±0.5	5.0±0.7	4.2±0.7	3.6±0.7
$\theta$ (°)	19°2±0°8	189°±8°	132°9±1°9	244°6±0°8	189°9±0°4	199°±7°
$\Delta F_{090M}$	0.88±0.03	1.6±0.4	...	0.21±0.10	...	...
$\Delta F_{110W}$	0.526±0.015	0.8±0.5 <sup>a</sup>	0.4±0.2 <sup>a</sup>	0.06±0.04	0.31±0.04	...
$\Delta F_{170M}$	0.820±0.013	0.9±0.6 <sup>a</sup>	0.4±0.3 <sup>a</sup>	1.030±0.019	0.461±0.016	...
F110W (A)	15.80±0.05	17.11±0.18	17.14±0.10	17.81±0.05	17.15±0.05	...
(B)	16.33±0.05	17.9±0.3	17.54±0.13	17.87±0.05	17.47±0.05	...
F170M (A)	14.04±0.05	15.31±0.19	16.21±0.13	16.19±0.05	16.98±0.05	...
(B)	14.86±0.05	16.2±0.4	16.61±0.18	17.22±0.05	17.44±0.05	...
F110W-F170M (A)	1.76±0.07	1.8±0.3	0.93±0.16	1.63±0.07	0.17±0.07	...
(B)	1.47±0.07	1.7±0.5	0.9±0.2	0.66±0.07	0.03±0.07	...
Est. SpT	L6.5+T2 <sup>b</sup>	L6:+T4: <sup>b</sup>	T4:+T4:	T1+T5 <sup>b</sup>	T6.5+T7	
$\Delta M_{bol}$	0.72±0.13	0.9±0.6	0.4±0.2	0.49±0.13	0.31±0.12	
$M_{bol}$ (A)	15.77±0.16	...	...	16.5±0.7	...	
(B)	16.50±0.16	...	...	17.0±0.7	...	
T <sub>2</sub> /T <sub>1</sub>	0.847±0.013	0.81±0.11	0.91±0.05	0.894±0.015	0.931±0.014	
T <sub>eff</sub> <sup>c</sup> (K) (A)	1490±100	~1600	~1330	1260±210	~980	
(B)	1250±80	~1330	~1330	1130±190	~890	
$q$	0.78±0.02	0.74±0.15	0.87±0.07	0.84±0.02	0.90±0.02	
Est. Mass <sup>d</sup> (M <sub>☉</sub> ) (A)	0.039–0.062	0.042–0.077	0.029–0.073	0.025–0.076	0.019–0.065	
(B)	0.029–0.051	0.031–0.074	0.029–0.073	0.021–0.074	0.016–0.061	
Est. Period <sup>e</sup> (yr)	~19	~10	~18	~50	~45	

<sup>a</sup>Estimated flux ratios including systematic effects; see §4.1.

<sup>b</sup>Based on spectral decomposition; see §5.3.

<sup>d</sup>Based on Golimowski et al. (2004) T<sub>eff</sub>/spectral type relation, with the exception of SDSS 0423-0413 and SDSS 1021-0304, where T<sub>eff</sub>s are derived from measured M<sub>bol</sub>s and assumed radii of 0.095±0.10 R<sub>☉</sub>.

<sup>d</sup>Based on ages of 0.5–5.0 Gyr (with the exception of SDSS 0423-0414, where 0.5–1.7 Gyr is assumed), estimated T<sub>eff</sub>s (except SDSS 0423-0414 and SDSS 1021-0304, where M<sub>bol</sub> is used) and the evolutionary models of Burrows et al. (1997).

<sup>e</sup>Assuming semimajor axes  $a = 1.26\rho$  (Fischer & Marcy 1992).

TABLE 6  
FAINT SOURCE DETECTION LIMITS FOR UNRESOLVED TARGETS.

Object (1)	Distance <sup>a</sup> (pc) (2)	$0''.04 \lesssim \rho \lesssim 0''.2$		$0''.2 \lesssim \rho \lesssim 1''.0$		$\rho_{min}$ (AU) (7)
		$\Delta F_{110W}$ (mag) (3)	$q$ (4)	$\Delta F_{110W}$ (mag) (5)	$q$ (6)	
SDSS 0151+1244	21.3±1.4	3.1	0.34	5.3	0.16	0.9
SDSS 0207+0000	29±8	2.8	0.38	3.8	0.27	1.2
2MASS 0243–2453	10.6±0.5	3.1	0.34	4.6	0.20	0.5
2MASS 0348–6022	~7	3.1	0.34	5.4	0.15	0.3
2MASS 0415–0935	5.75±0.10	3.2	0.33	6.0	0.12	0.2
2MASS 0516–0445	~19	3.3	0.32	5.9	0.13	0.8
2MASS 0755+2212	~20	3.5	0.29	5.8	0.13	0.9
SDSS 0837–0000	29±12	3.4	0.31	3.7	0.28	1.2
SDSS 1110+0116	~23	3.0	0.35	5.3	0.16	1.0
2MASS 1217–0311	11.0±0.2	3.1	0.34	5.3	0.16	0.5
SDSS 1254–0122	13.7±0.4	3.5	0.29	6.5	0.10	0.6
2MASS 1503+2525	~9	3.1	0.34	6.5	0.10	0.4
SDSS 1624+0029	10.9±0.2	3.1	0.34	6.0	0.12	0.5
SDSS 1750+1759	28±4	3.0	0.35	4.6	0.20	1.2
2MASS 2228–4310	~13	3.2	0.33	5.7	0.14	0.6
2MASS 2254+3123	~19	2.9	0.36	5.3	0.16	0.8
2MASS 2339+1352	~26	3.5	0.29	5.6	0.14	1.1

NOTE. — Given values are  $3\sigma$  detection limits for a single PSF subtraction from individual calibration images, separated into the core/first Airy ring region ( $\rho \lesssim 0''.2$ ) and the background-dominated region ( $\rho \gtrsim 0''.4$ ). Mass ratio ( $q$ ) limits assume  $\Delta F_{110W} \sim \Delta M_{bol}$  and Eqn. 6.

<sup>a</sup>Distance estimates for objects without parallax measurements are based on apparent 2MASS  $J$ -band magnitudes and the  $M_J$ /spectral type relation of Tinney, Burgasser & Kirkpatrick (2003).

TABLE 7  
L/T TRANSITION BINARIES.

Name (1)	Spectral Types		Distance <sup>a</sup> (pc) (4)	Separation		Period (yr) (7)	Note (8)
	(A) (2)	(B) (3)		( $''$ ) (5)	(AU) (6)		
SDSS J042348.57–041403.5	L6	T2	15.2±0.4	0''164±0''005	2.49±0.07	~19	1,2
2MASS J05185995–2828372	L6:	T4:	~34	0''051±0''012	1.8±0.5	~10	3,4
2MASS J08503593+1057156	L6	T:	26±2	0''16±0''010	4.4±0.4	~43	5
2MASS J09201223+3517429	L6.5	T:	~21	0''07±0''010	1.5±0.5	~6	5
Gliese 337C	L8	T:	20.5±0.4	0''53±0''03	10.9±0.7	~150	6,7
SDSS J102109.69–030420.1	T1	T5	29±4	0''172±0''005	5.0±0.7	~48	2,4
Epsilon Indi B	T1	T6	3.626±0.013	0''732±0''002	2.654±0.012	~15	7,8
SDSS J153417.05+161546.1	T1.5	T5.5	~36	0''110±0''005	3.9±0.6	~28	9
2MASS J17281150+3948593	L7	T:	~23	0''131±0''003	3.0±0.5	~35	10
2MASS J22521073-1730134	L6	T2:	14±3	0''130±0''002	1.8±0.4	~9	11

REFERENCES. — (1) Burgasser et al. (2005b); (2) Vrba et al. (2004); (3) Cruz et al. (2004); (4) This paper; (5) Reid et al. (2001); (6) Burgasser et al. (2005a); (7) ESA (1997); (8) McCaughrean et al. (2004); (9) Liu et al. (2006); (10) Gizis et al. (2003); (11) Reid et al. (2006b).

<sup>a</sup>Parallax distance measurements from ESA (1997) and Vrba et al. (2004) are given with uncertainties, all others are spectrophotometric distance estimates from the discovery references.

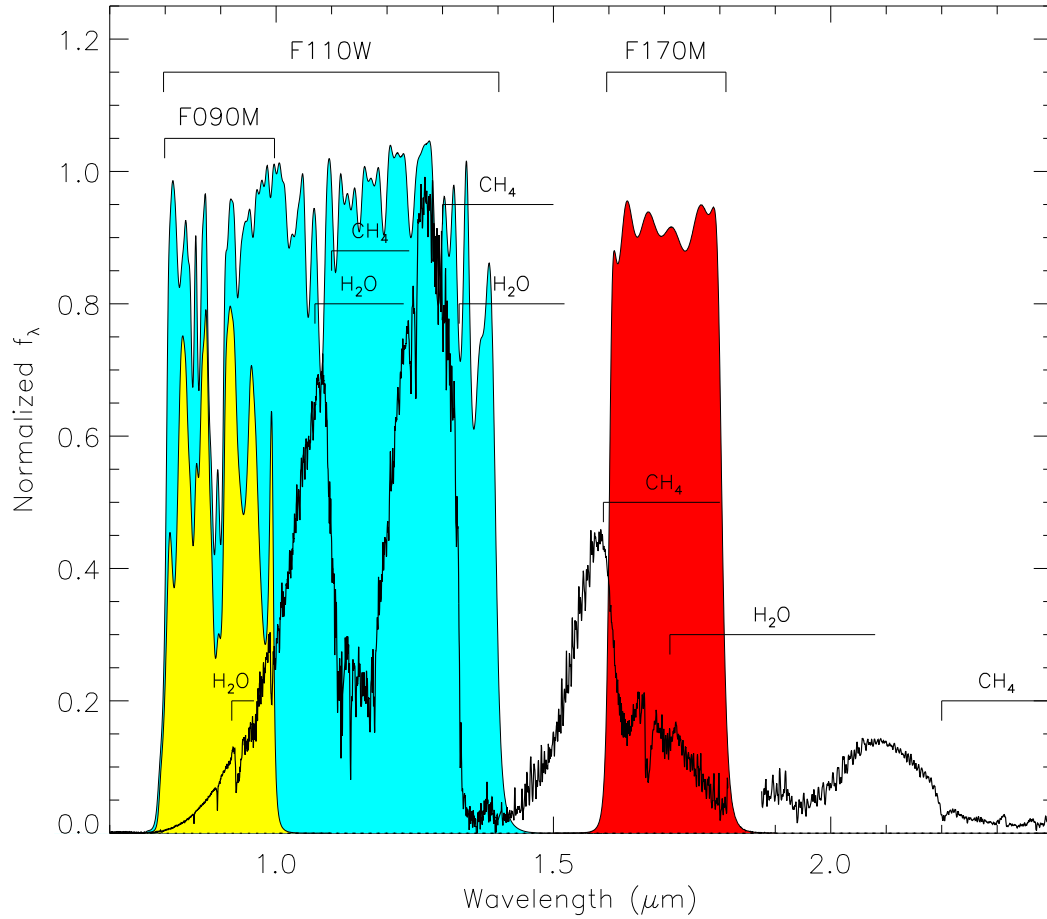


FIG. 1.— NIC1 F090M (yellow), F110W (blue) and F170M (red) filter transmission profiles overlaid on the red optical and near infrared spectrum of 2MASS 1503+2525 (Burgasser et al. 2003a, 2004a). Spectral data are normalized at 1.27  $\mu\text{m}$ . Filter transmission profiles are preflight measurements and do not include the NIC1 detector quantum efficiency or optical element response curves. Key  $\text{H}_2\text{O}$  and  $\text{CH}_4$  bands present in the spectra of T dwarfs are indicated.

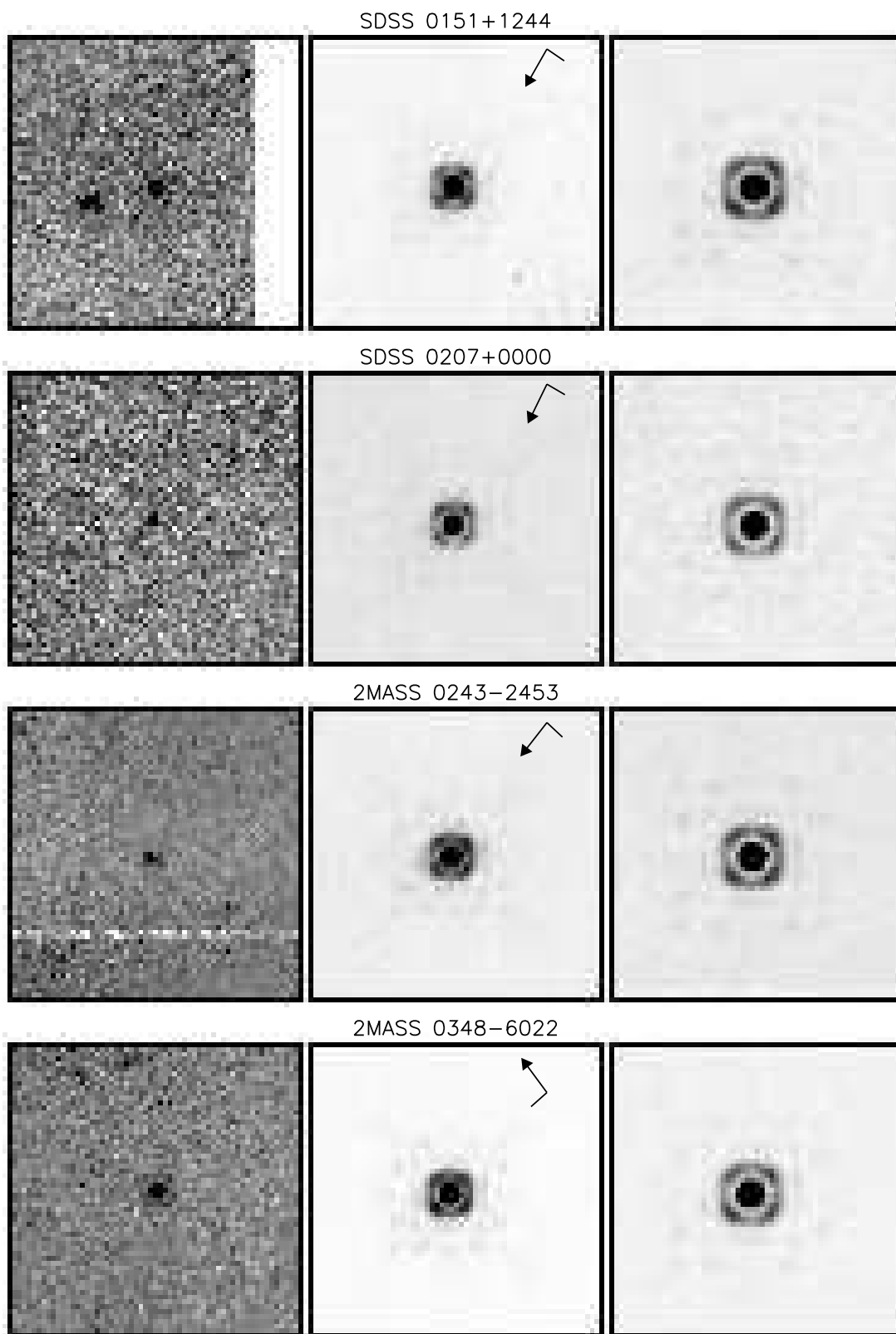


FIG. 2.— NICMOS F090M (left), F110W (center) and F170M (right) images of T dwarfs observed in this study. Subsections of  $2''.5 \times 2''.5$  in size are shown on a logarithmic scale. Orientations North (arrow) and East (line) are indicated in the center panel.

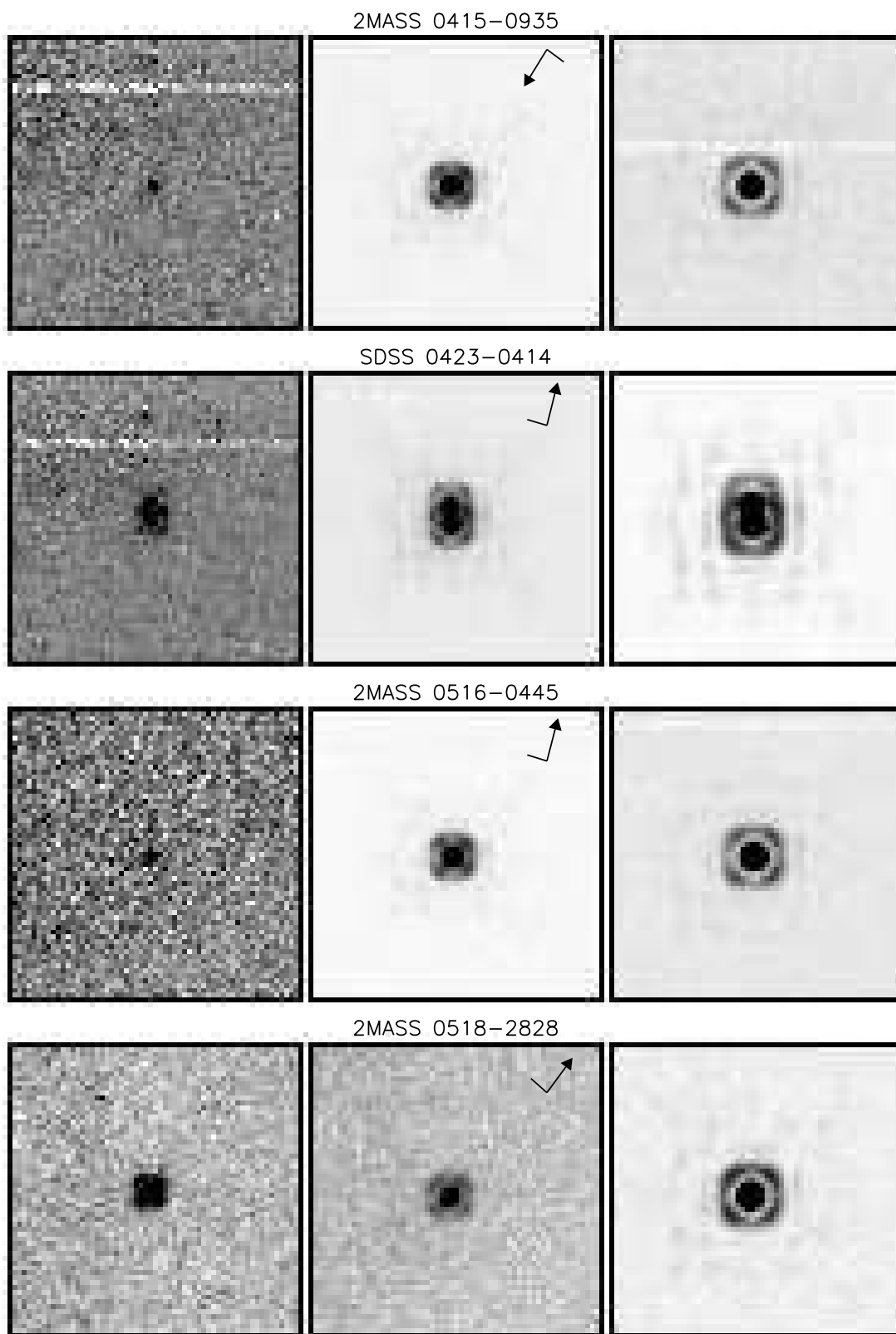
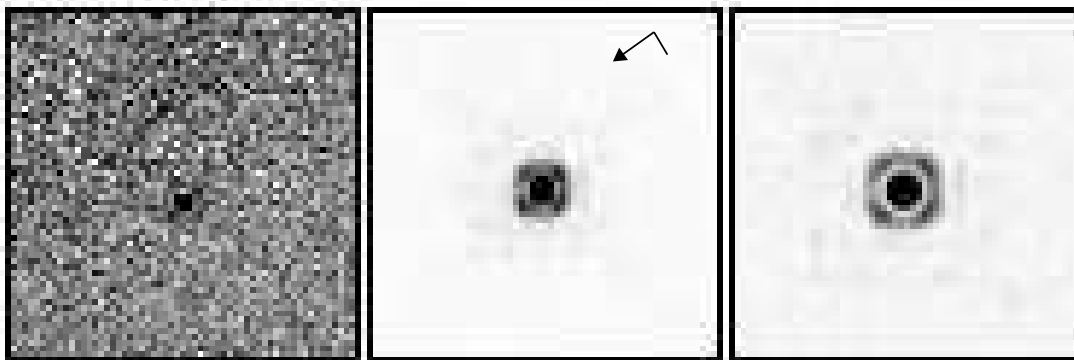
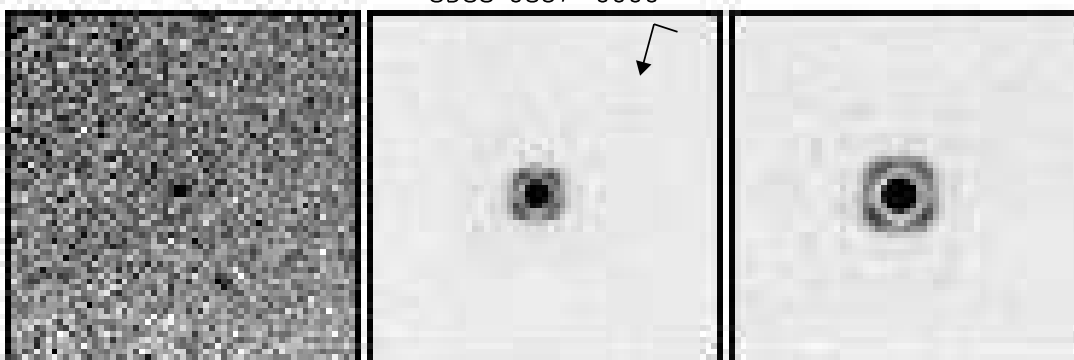


Fig. 2. — Continued.

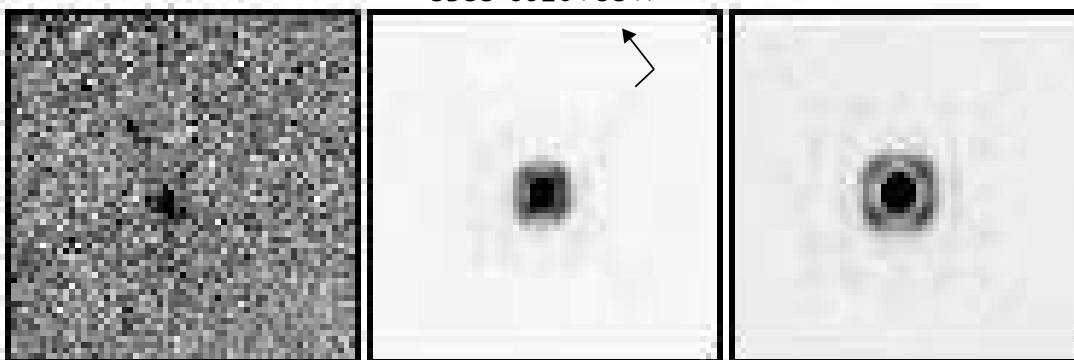
2MASS 0755+2212



SDSS 0837-0000



SDSS 0926+5847



SDSS 1021-0304

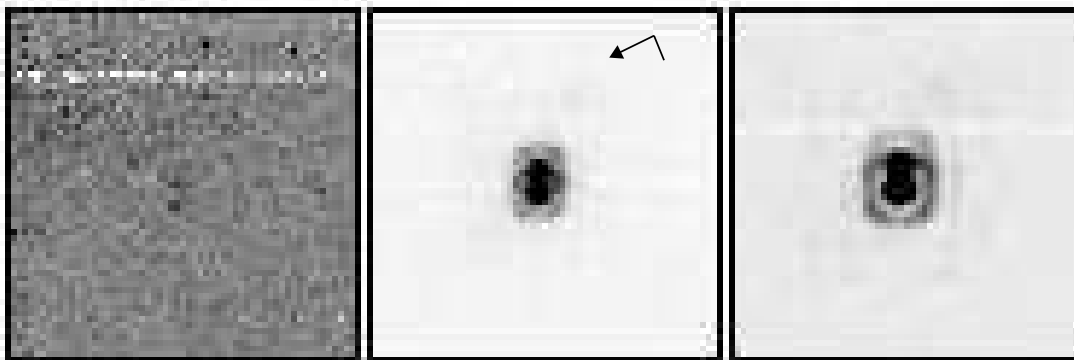
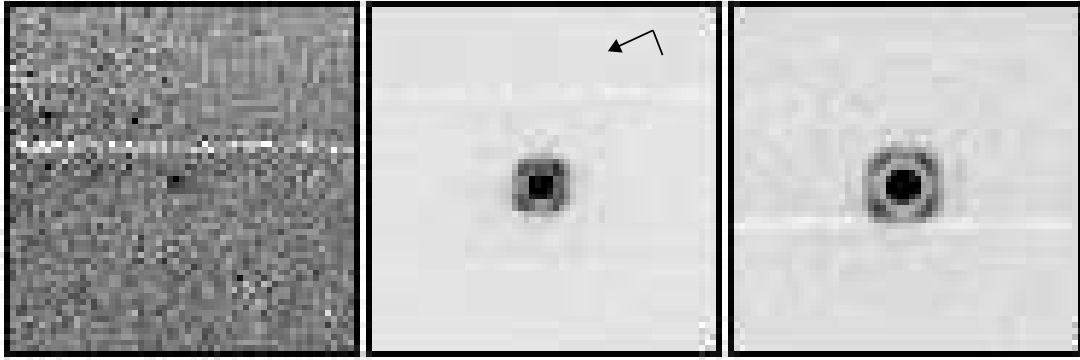
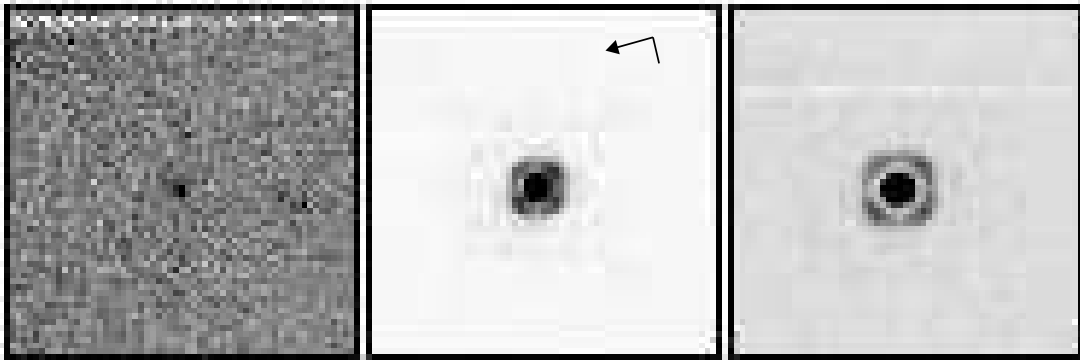


Fig. 2. — Continued.

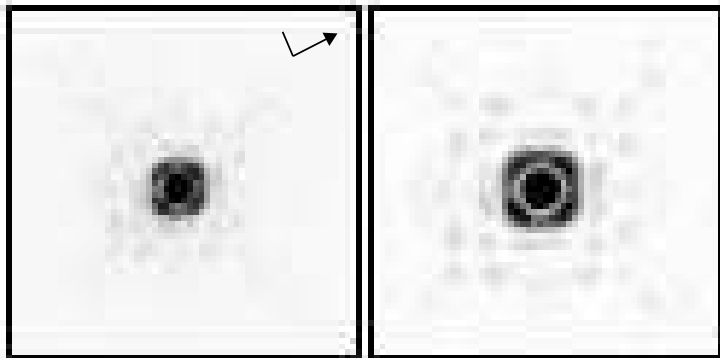
SDSS 1110+0116



2MASS 1217-0311



SDSS 1254-0122



2MASS 1503+2525

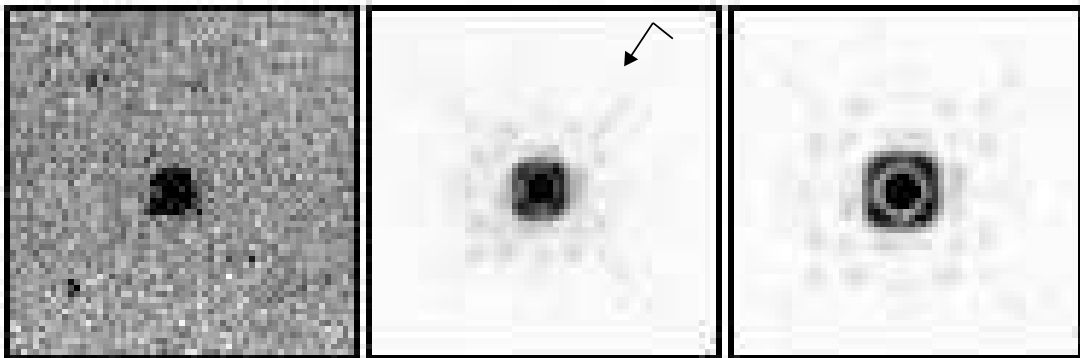
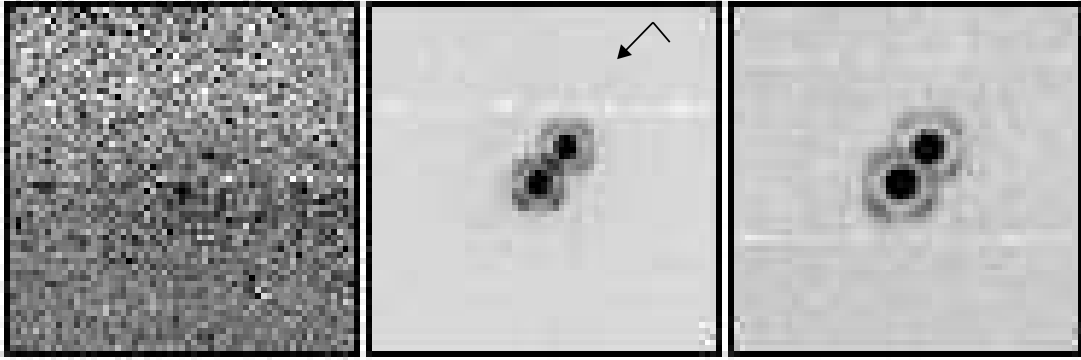
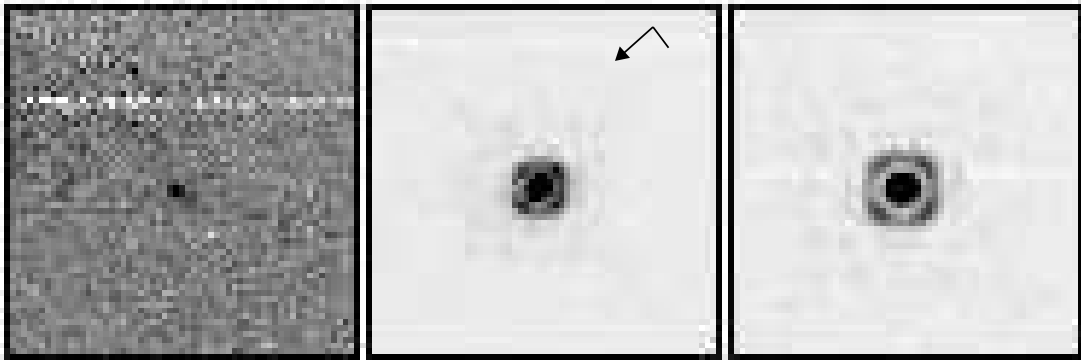


Fig. 2. — Continued.

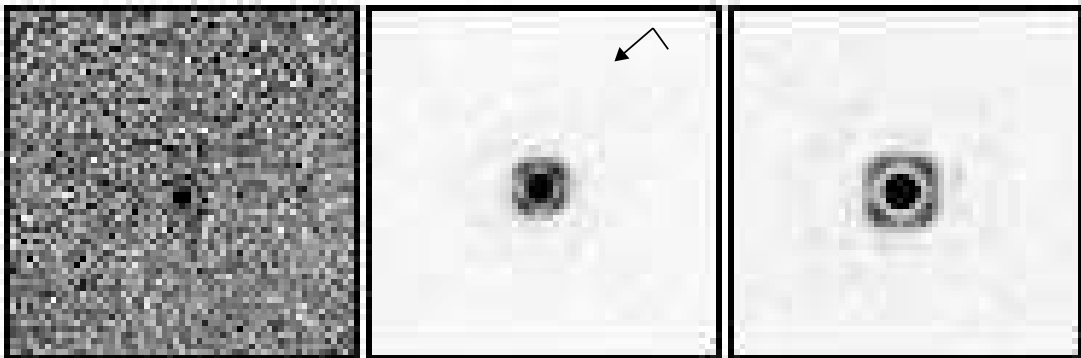
2MASS 1553+1532



SDSS 1624+0029



SDSS 1750+1759



2MASS 2228-4310

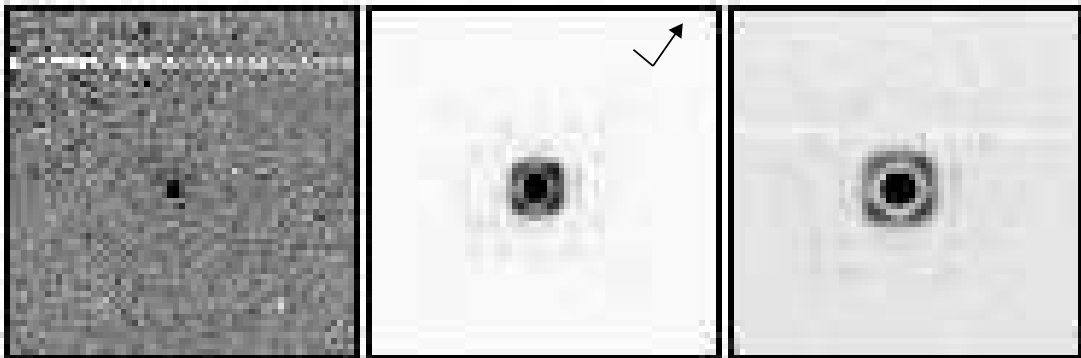
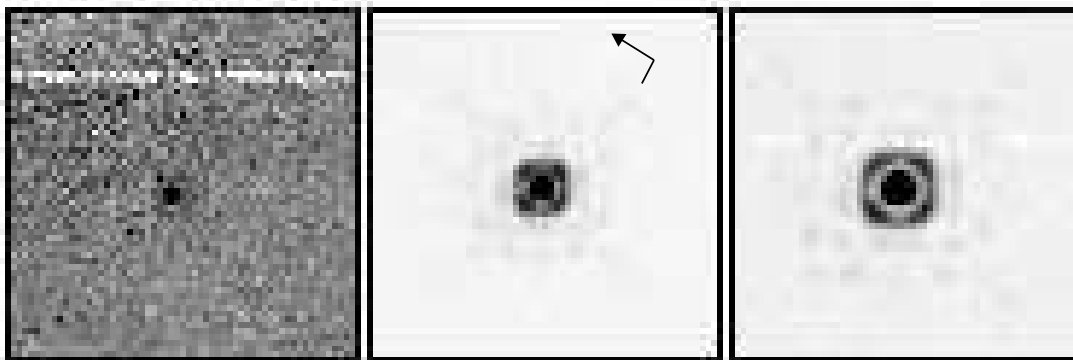


Fig. 2. — Continued.

2MASS 2254+3123



2MASS 2339+1352

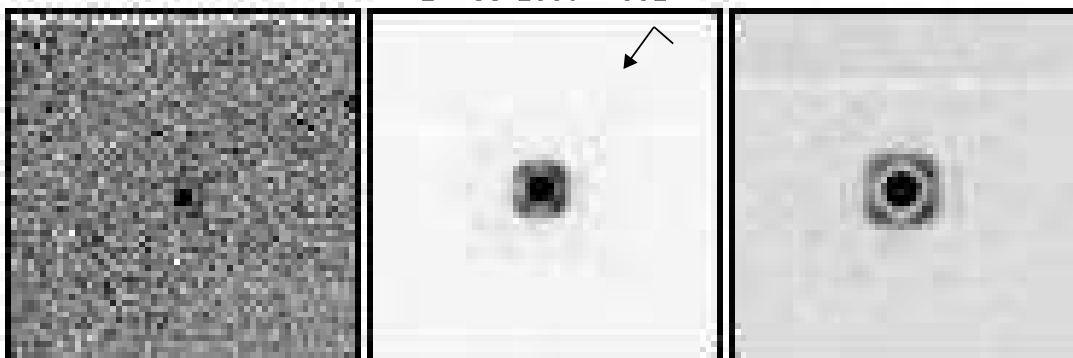


Fig. 2. — Continued.

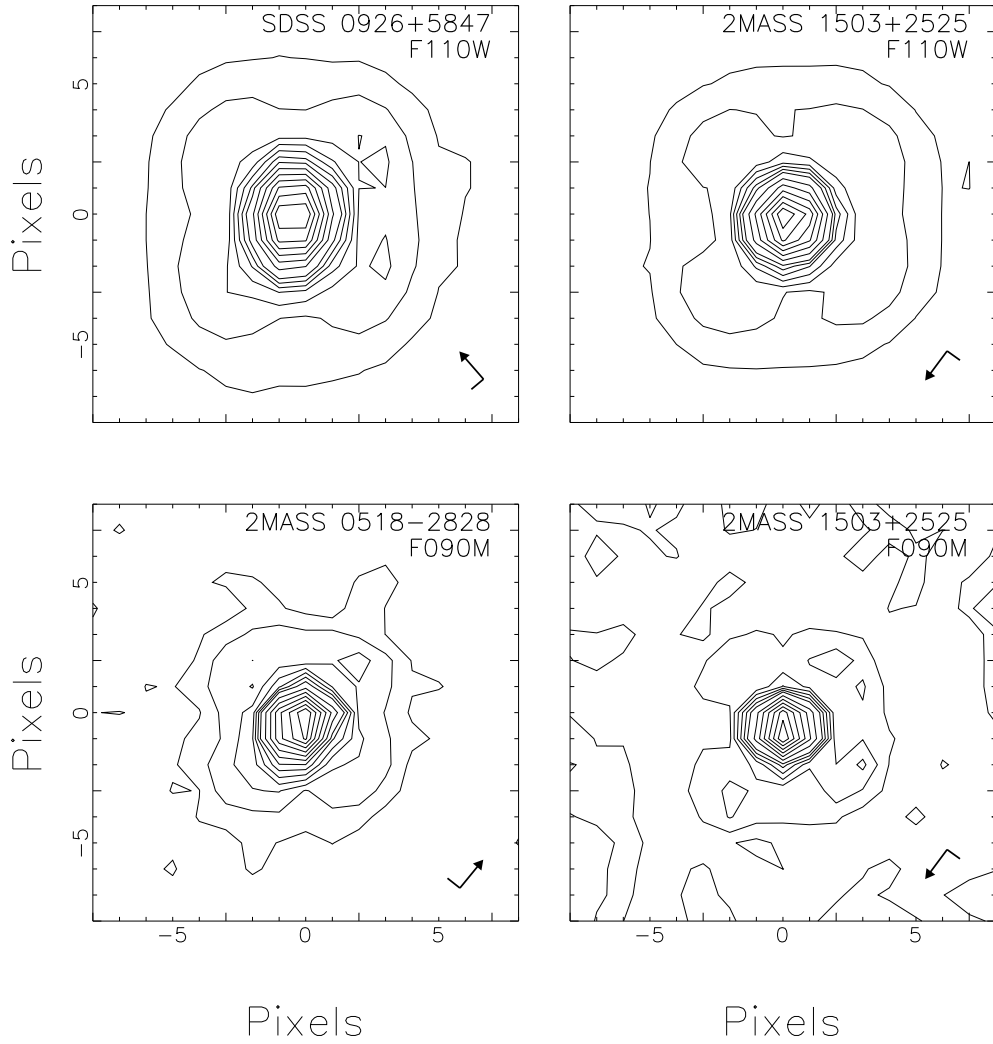


FIG. 3.— Contour plots of F110W images of the central  $0''.9 \times 0''.9$  regions around SDSS 0926+5847 (top left) and 2MASS 1503+2525 (top right), and F090M images of 2MASS 0518-2828 (bottom left) and 2MASS 1503+2525 (bottom right). Lines indicate isofluxes of 0.01, 0.05, 0.1, 0.15, 0.2, 0.25, 0.3, 0.4, 0.5, 0.6, 0.7, 0.8, 0.8, 0.9 and 1.0 times the peak source flux. Orientations (North and East) for each image are indicated in the lower right corners.

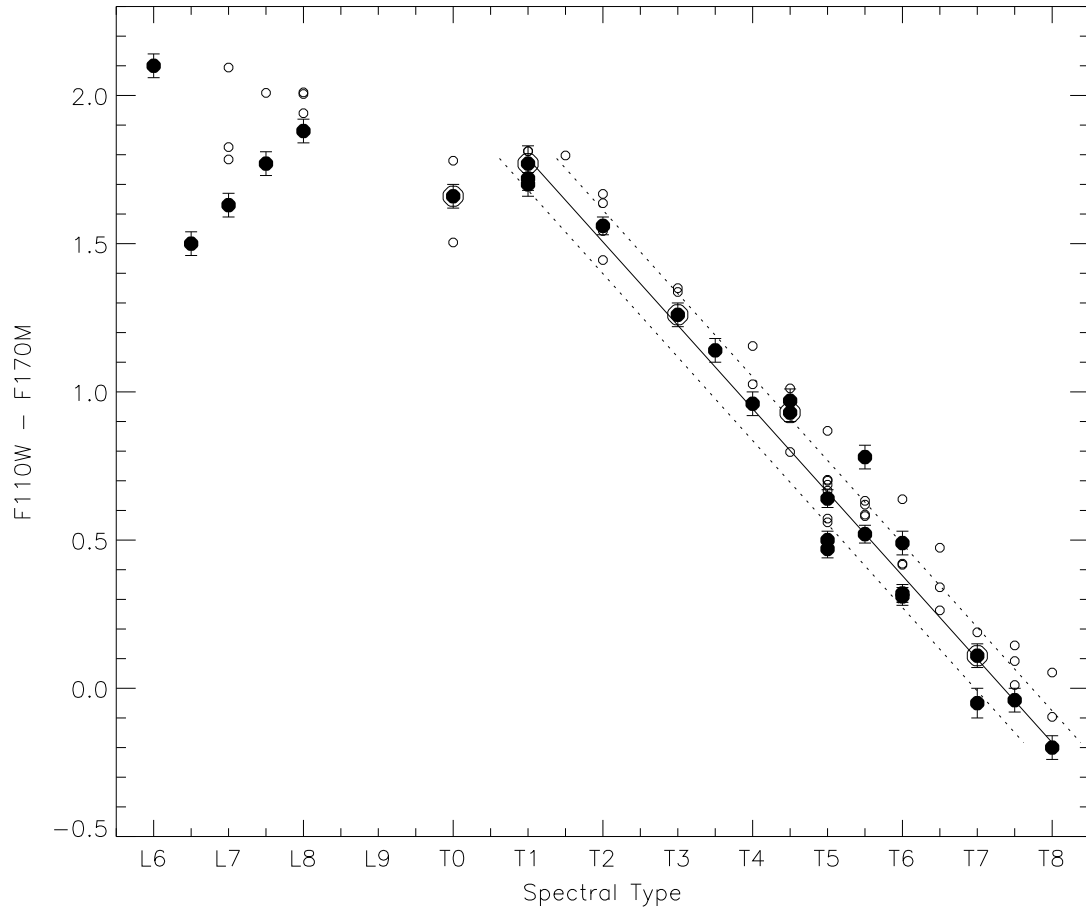


FIG. 4.—  $F110W-F170M$  colors versus spectral type for subtypes L6 to T8. L dwarf classifications are based on optical spectra (e.g., Kirkpatrick et al. 1999); T dwarf classifications are based on near infrared spectra (e.g., Burgasser et al. 2006). Photometry from this program and Reid et al. (2006a) are shown as solid circles with error bars; multiple sources are encircled. Spectrophotometric colors measured from low resolution near infrared data from Burgasser et al. (2006a) are shown as small open circles. A linear fit to the photometric data of unresolved objects is indicated by the solid line;  $\pm 1\sigma$  scatter about this relation are indicated by the dotted lines.

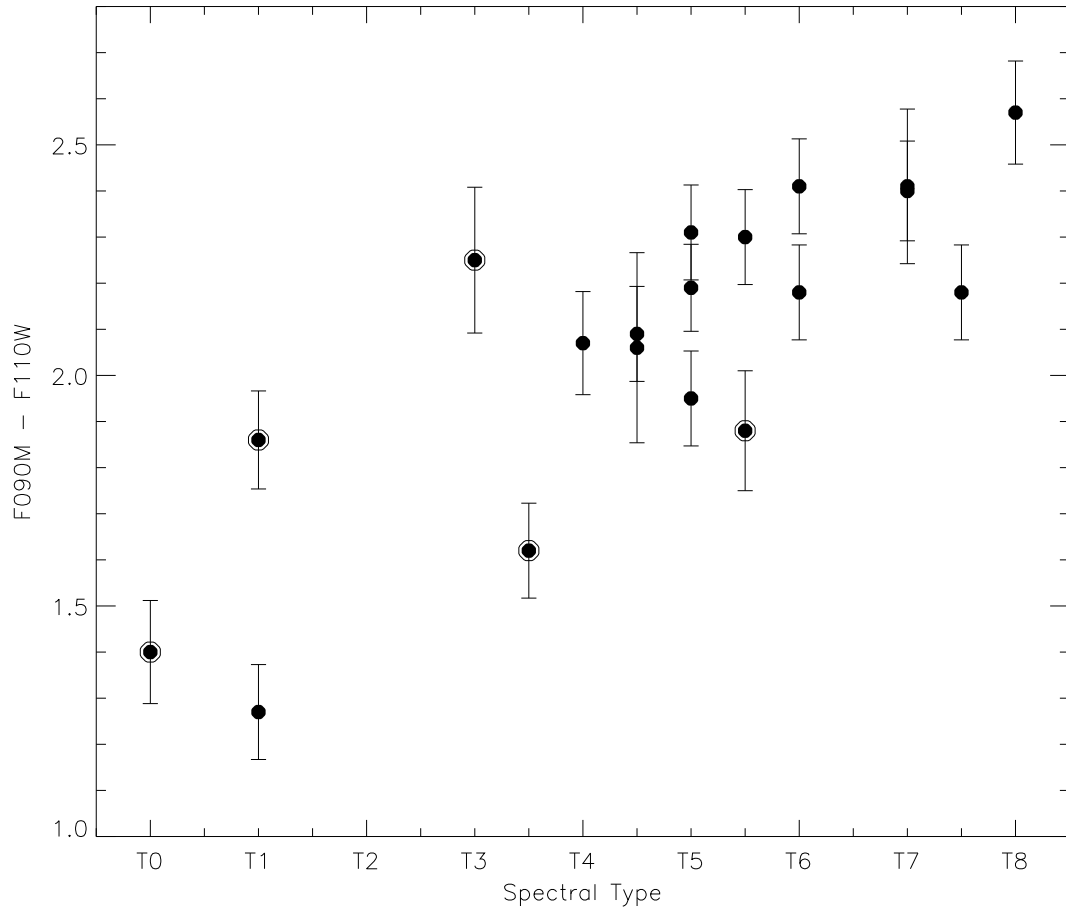


FIG. 5.—  $F_{090M}-F_{110W}$  colors versus spectral type for T dwarfs in our sample. Symbols are the same as in Figure 4.

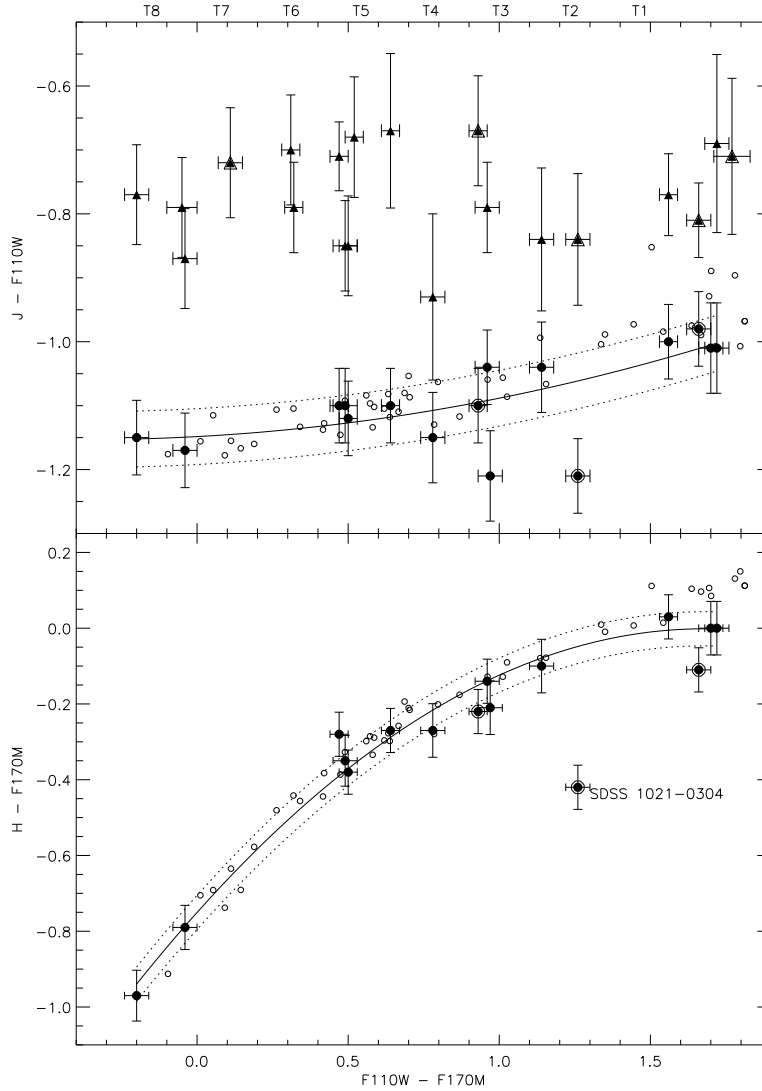


FIG. 6.— *Top:*  $J - F110W$  versus  $F110W - F170M$  color for sources in our sample. Solid circles indicate colors on the MKO system, solid triangles indicate colors on the 2MASS system. Multiple sources are encircled. Spectrophotometric colors on the MKO system measured from low resolution near infrared data are shown as small open circles. A polynomial fit to the MKO photometry of unresolved sources is indicated by the solid line;  $\pm 1\sigma$  scatter about this relation are indicated by the dotted lines. *Bottom:*  $H - F170M$  color versus  $F110W - F170M$  color for sources in our sample. Symbols are the same as in the top panel, and only MKO photometry are shown. A polynomial fit to photometry for unresolved sources is indicated by the solid line;  $\pm 1\sigma$  scatter about this relation are indicated by the dotted lines. The discrepant (multiple) source SDSS 1021-0304 is labeled.

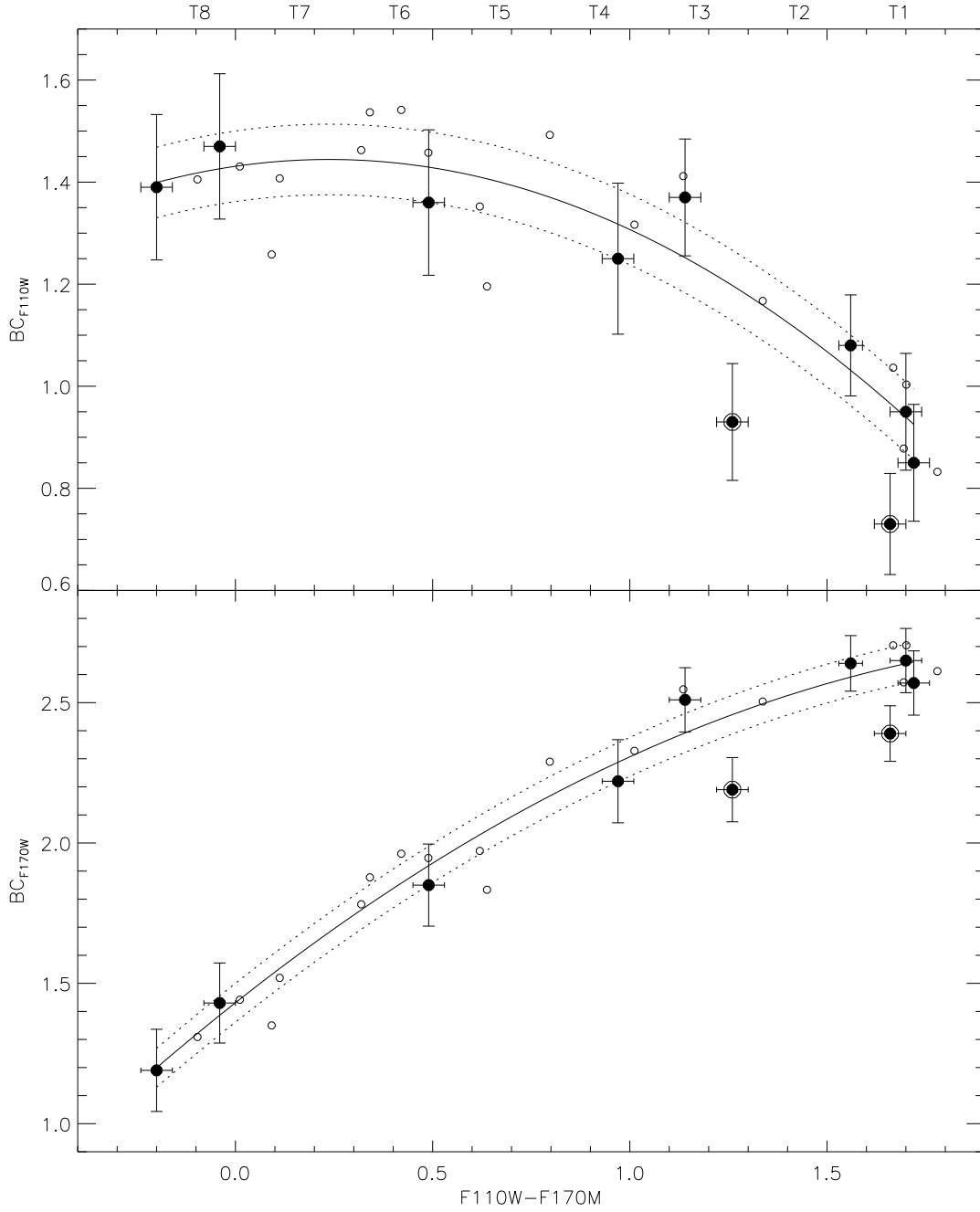


FIG. 7.—  $F110W$  and  $F170M$  bolometric corrections (BC) as a function of  $F110W - F170M$  color. BC values are based on  $K$ -band bolometric corrections from Golimowski et al. (2004) and MKO  $K$ -band photometry for sources in our sample. Spectrophotometric BCs measured from low resolution near infrared data from Burgasser et al. (2006a) are shown as small open circles. Polynomial fits to the BCs of unresolved sources observed in this program are indicated by the solid lines;  $\pm 1\sigma$  scatter about these relations are indicated by the dotted lines.

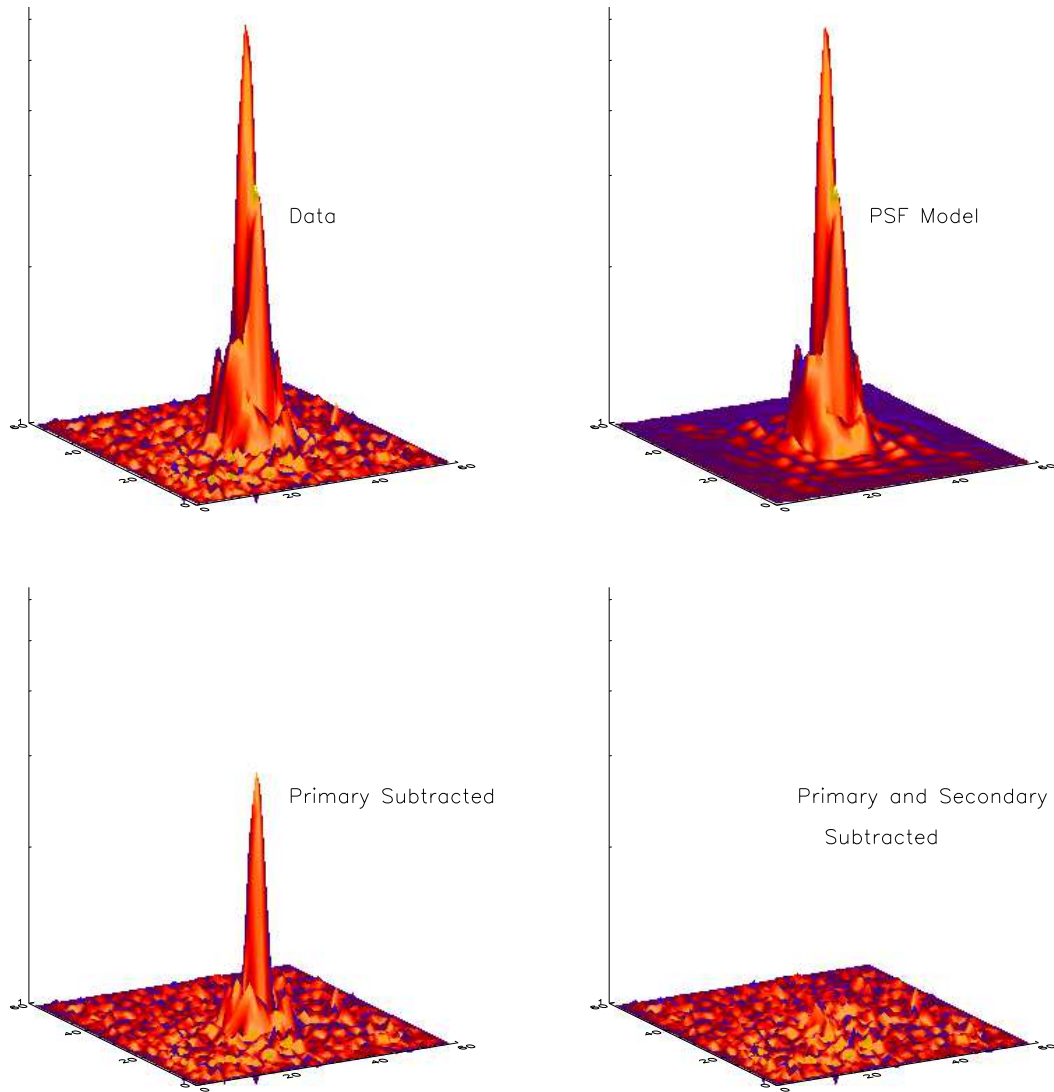


FIG. 8.— Surface plots illustrating PSF fits to F170M imaging data of the SDSS 1021-0304 binary. Shown clockwise from upper left are  $2''.5 \times 2''.5$  subsections of imaging data, the best fitting PSF model, subtraction of the primary PSF model from the data, and subtraction of the full PSF model from the data. All four plots are normalized to a common logarithmic scale; average residuals in the final subtraction are 0.4% of the peak source flux.

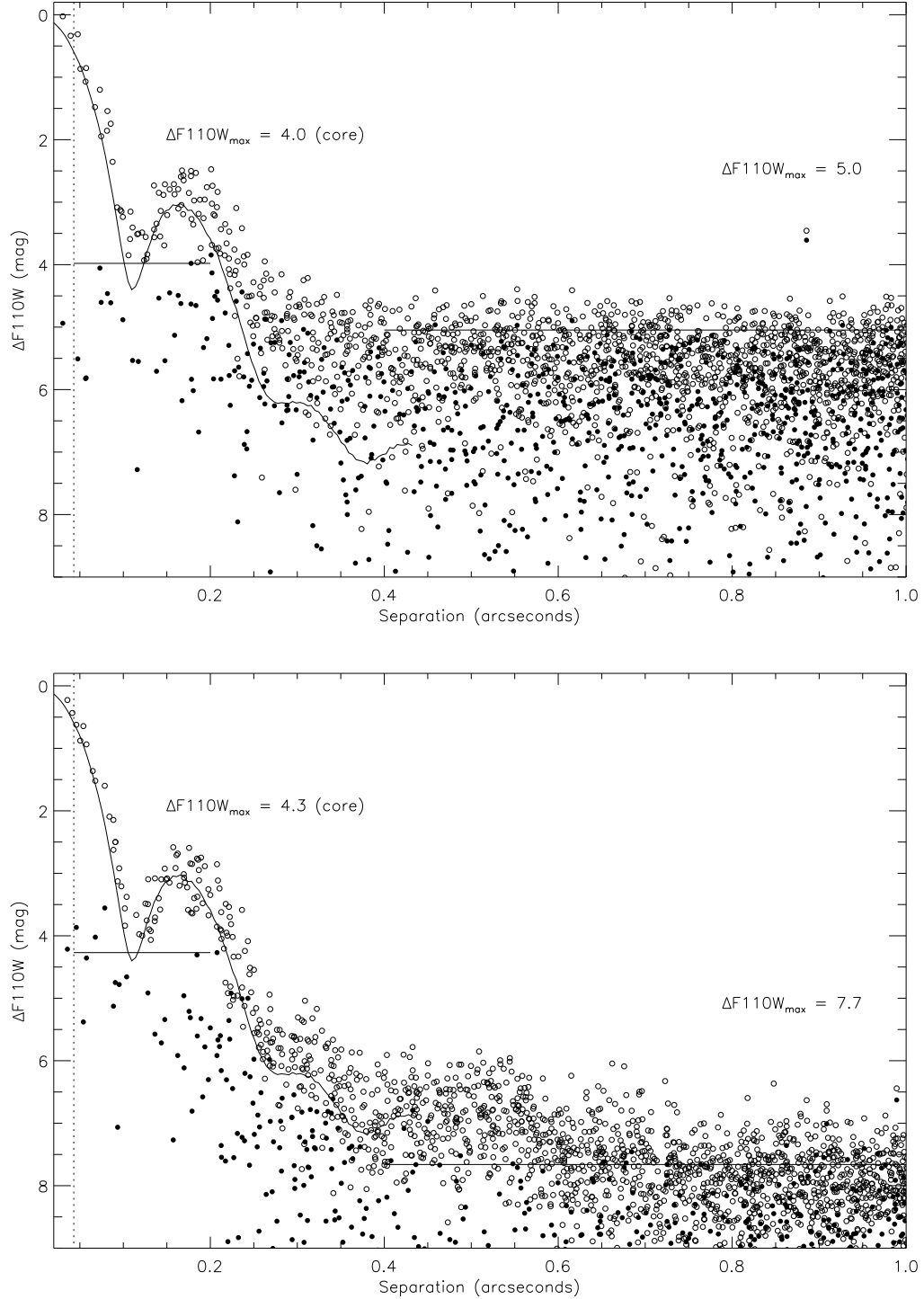


FIG. 9.— Sensitivity limits for faint companions around the faintest and brightest unresolved sources, SDSS 0207+0000 (top) and 2MASS 1503+2525 (bottom). Open circles trace the relative brightness profile with respect to the peak PSF in the original NICMOS image; filled circles trace the brightness profile after PSF subtraction. The solid lines trace the radial profile of an oversampled model PSF from Tiny Tim. Residuals in the PSF core ( $0''.04$ – $0''.2$ ) after model subtraction are consistently  $\sim 4$  mag below the peak primary flux. The far wing sensitivity is dominated by background noise.

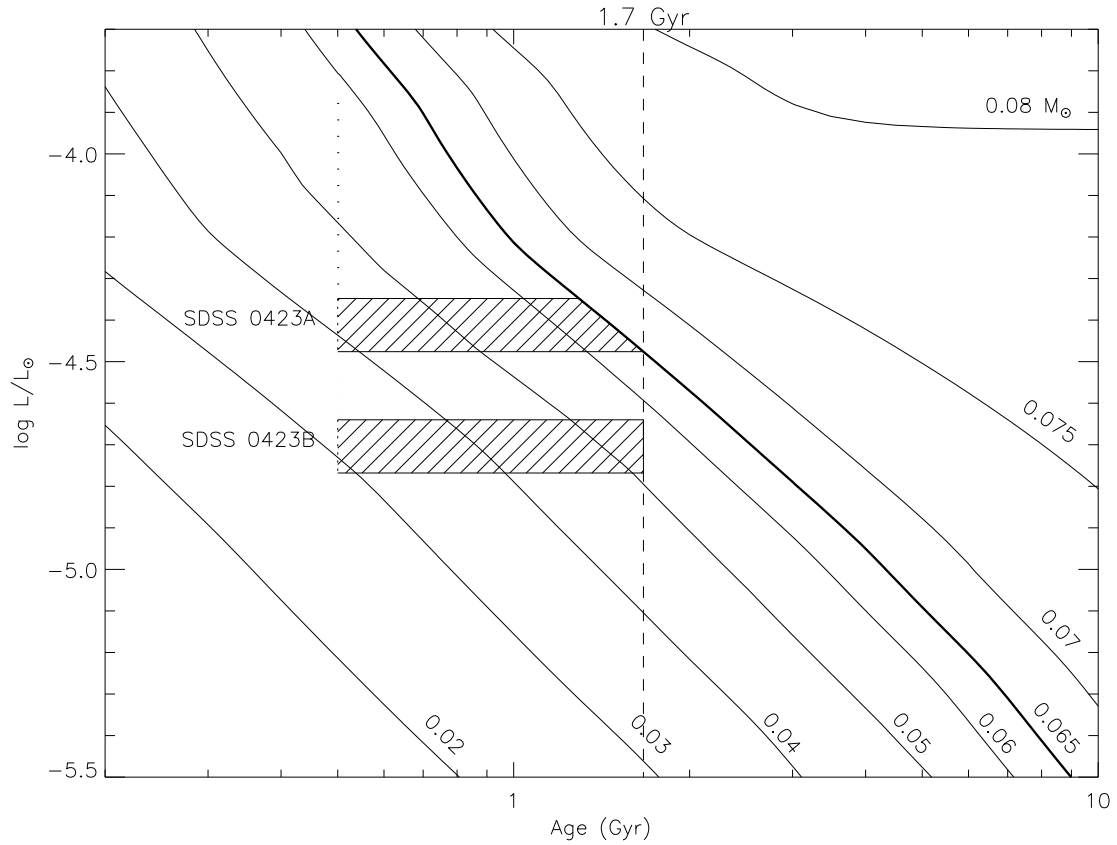


FIG. 10.— Comparison of component bolometric luminosities for SDSS 0423-0414 to theoretical evolutionary models. Isomass evolutionary tracks are indicated by lines and labeled (in Solar masses). The 1% Li depletion limit is indicated by the thick line, and effectively lies along the 0.065  $M_{\odot}$  track for the ages shown. A minimum age for the system of  $\sim 0.5$  Gyr is based on the absence of notable low surface gravity features in the optical and/or near infrared spectrum of this object. A maximum age of 1.7 Gyr is constrained by the detection of strong Li I absorption, most likely from the primary component.

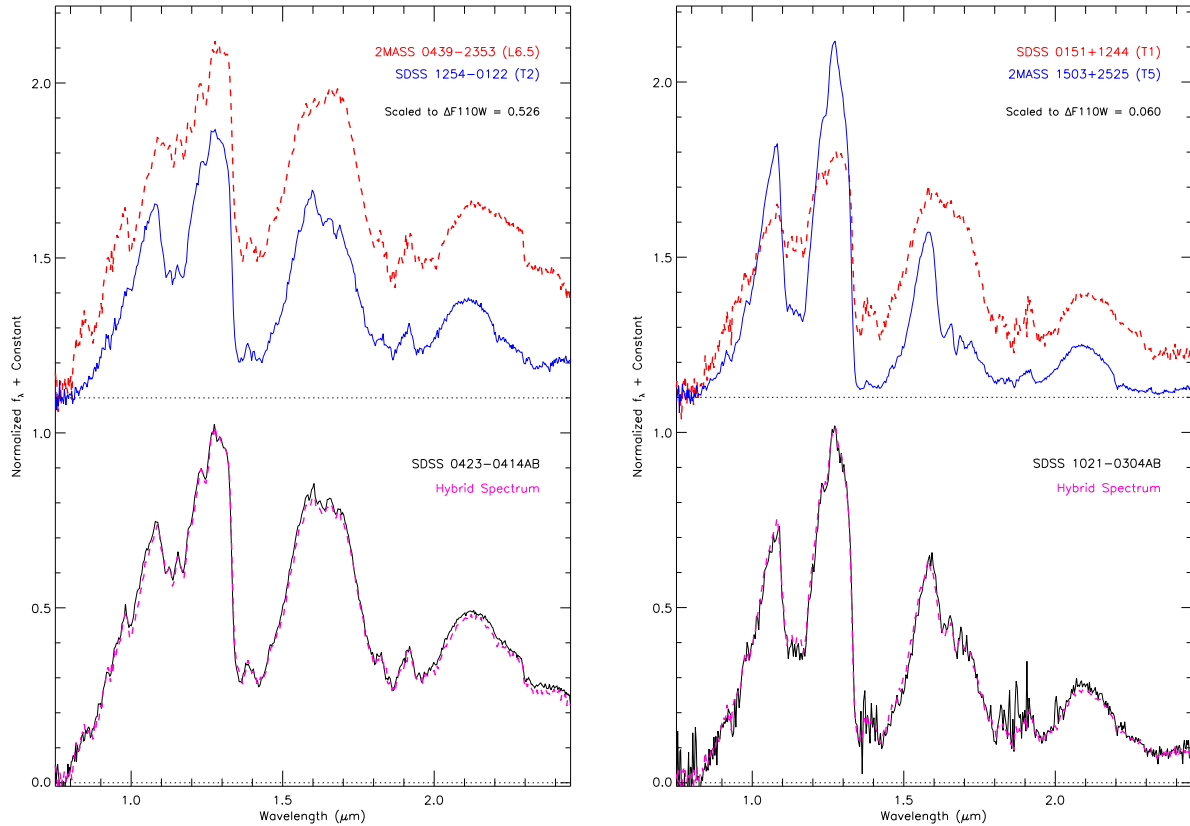


FIG. 11.— Spectral decomposition of SDSS 0423-0414 (left) and SDSS 1021-0304 (right). The top of each panel shows the best fit spectral standards to the primary (red dashed line) and secondary (blue solid line) of each binary, normalized and scaled to the relative F110W magnitudes as measured with NICMOS. The bottom of each panel compares the combined light spectrum of the binary (black solid line) to the hybrid spectrum of the two spectral components (purple dashed line), both normalized at  $1.27 \mu\text{m}$ . The agreement between the combined light and hybrid spectra is overall quite remarkable.

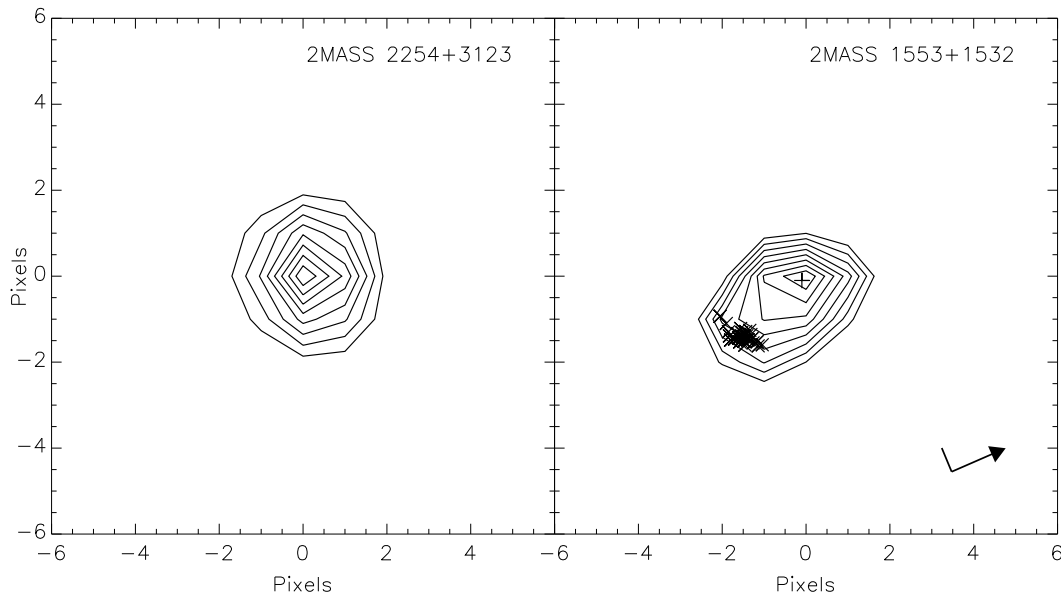


FIG. 12.— Contour plots for one set of NIRC  $K_s$ -band images of 2MASS 2254+3123 (left) and 2MASS 1553+1532 (right). The displayed boxes correspond to a  $1''.8 \times 1''.8$  area on the sky, and orientation for both images is indicated by the arrow (pointing north) in the right panel. Contour levels corresponding to 0.2, 0.3, 0.4, 0.5, 0.6, 0.7, 0.8 and 0.9 times the peak source flux are shown. Relative separations for the 42 best PSF fits to 2MASS 1553+1532 are indicated by the plus symbol (corresponding to the primary) and crosses (corresponding to the secondaries), and are consistent with a mean separation of  $0''.30 \pm 0''.02$  and position angle of  $199 \pm 7^\circ$ .

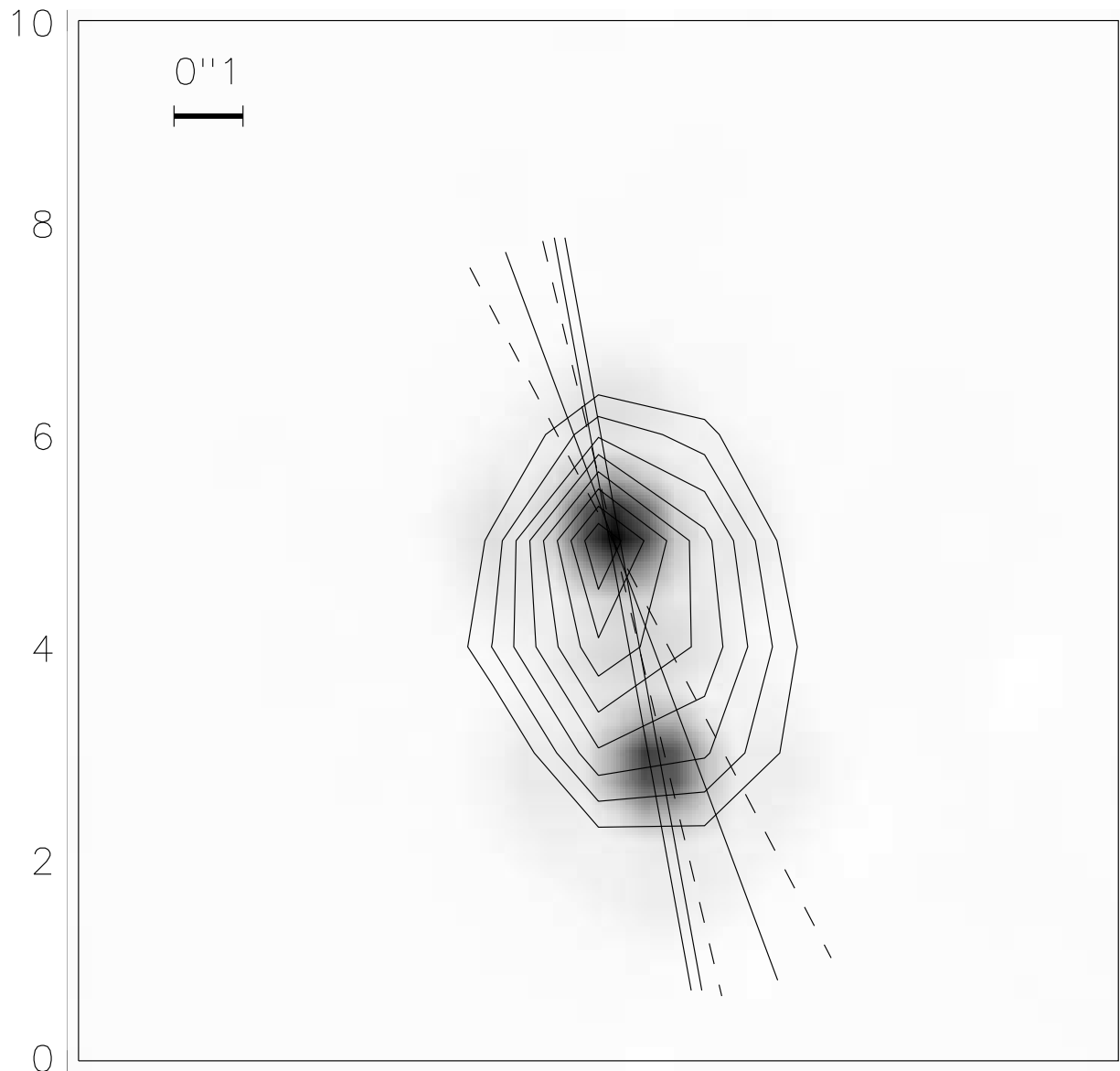


FIG. 13.— Comparison between NIRC  $K_s$ -band (contours) and *HST* F110W (greyscale) images of 2MASS 1553+1532. Both images are oriented with north up and east to the left, and angular scale is indicated in the upper left corner. The position angles between the primary and secondary as determined by PSF fitting are overlaid; the single line and dashed lines correspond to mean and  $1\sigma$  uncertainty as measured from the NIRC images, the double line corresponds to the best fit from the *HST* images. A slight rotation and expansion of the system between the two imaging epochs can be discerned.

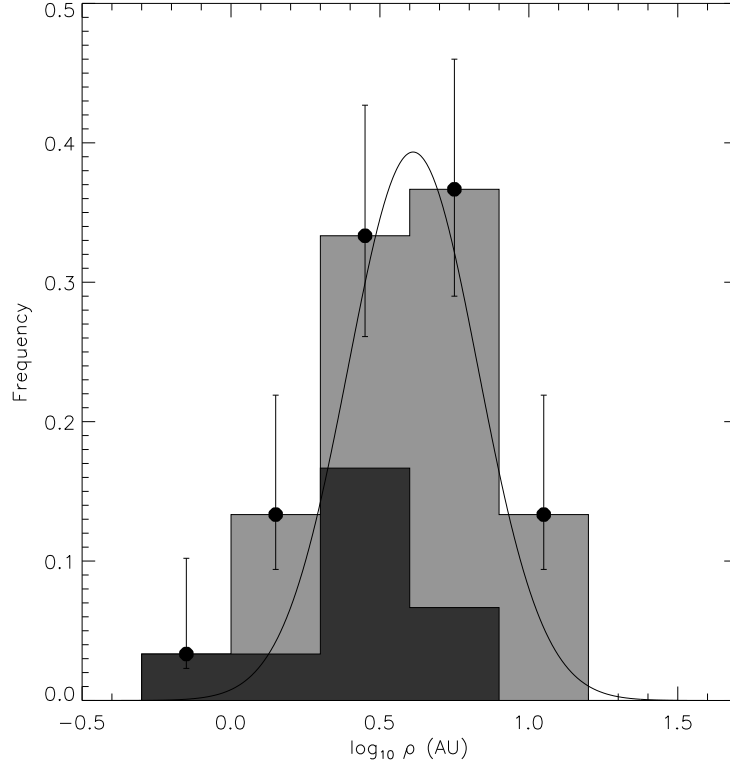


FIG. 14.— Projected separation distribution (light grey histogram) of 30 brown dwarf binaries identified in high resolution imaging studies by Martín et al. (1999); Leinert et al. (2001); Reid et al. (2001, 2006a); Potter et al. (2002); Bouy et al. (2003); Burgasser et al. (2003c); Gizis et al. (2003); McCaughrean et al. (2004); Burgasser et al. (2005a); Liu & Leggett (2005); Liu et al. (2006); and this study. Uncertainties based on counting statistics are indicated by error bars. The distribution exhibits a peak at  $\rho \approx 4$  AU ( $\log_{10} \rho = 0.6$ ) as derived from a Gaussian fit (solid line), although the decline at smaller separations may be the result of resolution limits in the imaging studies. Note that T dwarf binaries (dark grey histogram) have smaller projected separations on average as compared to all resolved brown dwarf binaries.

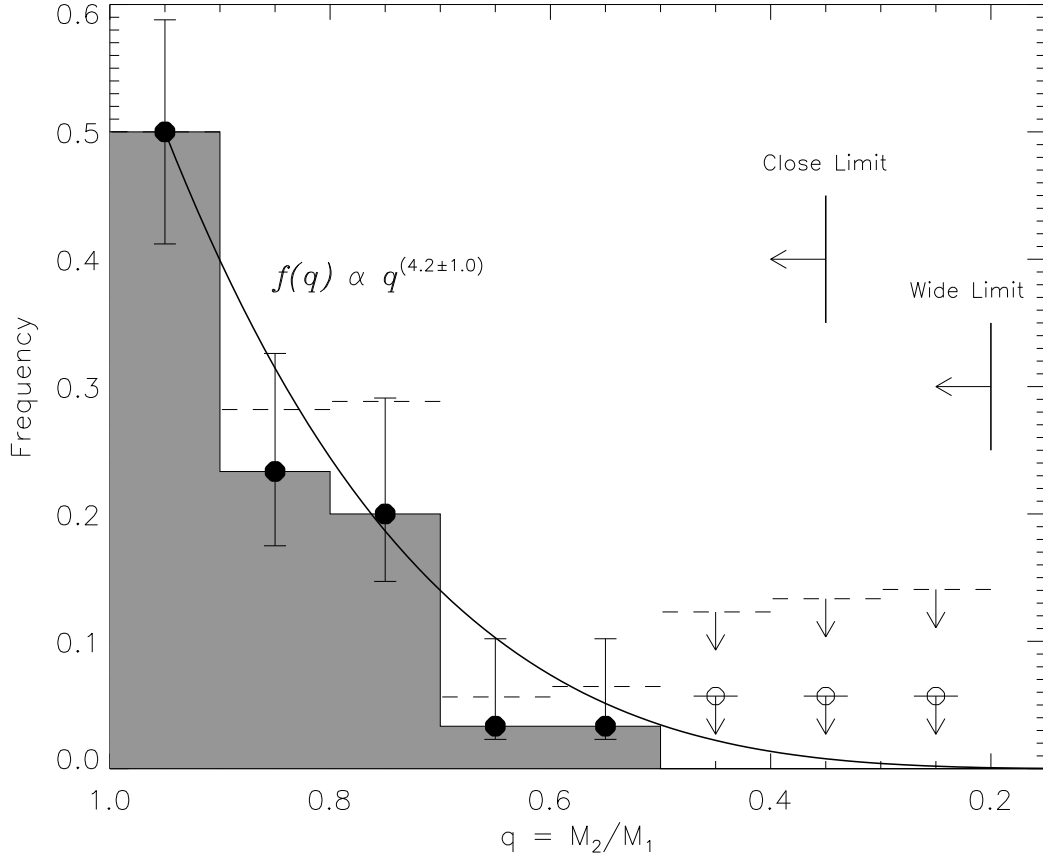


FIG. 15.— Mass ratio distribution of the 30 brown dwarf binaries from Figure 14. Uncertainties based on counting statistics are indicated by error bars, upper limits are indicated by open circles. Bias corrected values are shown by dashed lines. A power law fit to the bias-corrected values,  $f(q) \propto q^{(4.2 \pm 1.0)}$ , is shown by the thick solid line. Sensitivity limits at close ( $\rho \gtrsim 0''.04$ ) and wide ( $\rho \gtrsim 0''.2$ ) separations are indicated.

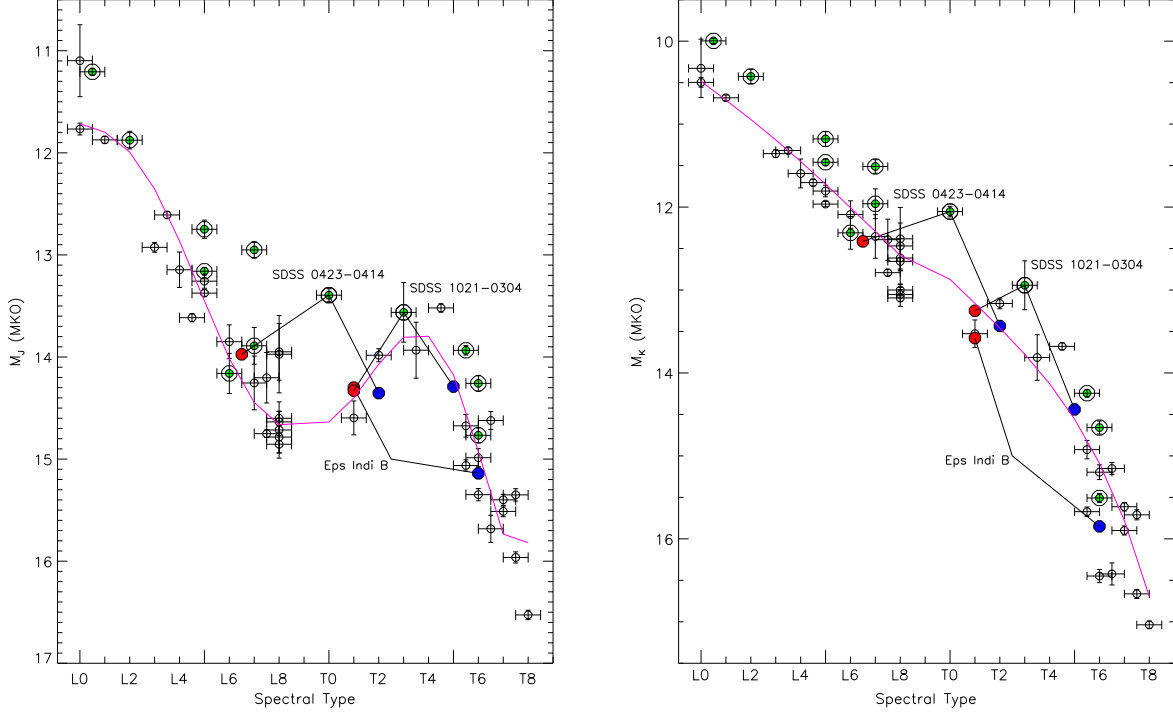


FIG. 16.— Absolute MKO  $J$ - (left) and  $K$ -band (right) magnitudes versus spectral type for field L and T dwarfs with parallax measurements (Dahn et al. 2002; Tinney, Burgasser & Kirkpatrick 2003; Vrba et al. 2004) and companions to nearby Hipparcos stars (Becklin & Zuckerman 1988; Nakajima et al. 1995; Burgasser et al. 2000b; Kirkpatrick et al. 2001; McCaughrean et al. 2004). Spectral types are based on optical data for the L dwarfs and near infrared data for the T dwarfs. Combined light photometry for known binaries are encircled. Primary (red circles) and secondary (blue circles) spectral types and magnitudes for the SDSS 0423-0414, SDSS 1021-0304 and Epsilon Indi B binaries are indicated. Absolute MKO magnitude/spectral type relations from Tinney, Burgasser & Kirkpatrick (2003) are shown by the solid curves.

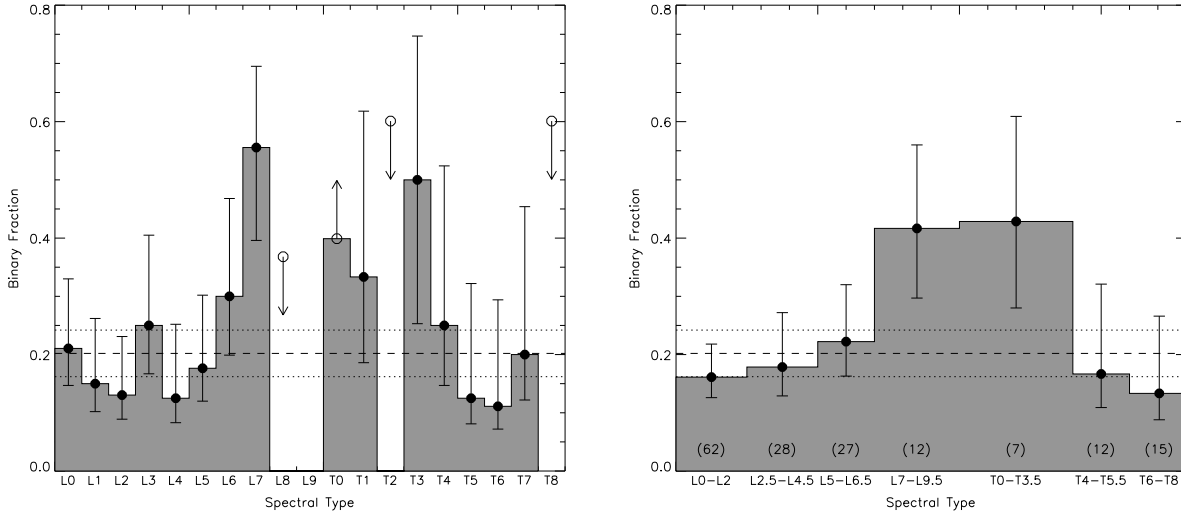


FIG. 17.— Observed binary fractions of L and T dwarfs as a function of spectral type. Data were compiled from the imaging surveys of Koerner et al. (1999); Martín et al. (1999); Reid et al. (2001, 2006a); Close et al. (2003); Bouy et al. (2003); Burgasser et al. (2003c); Gizis et al. (2003); and this study. Counting uncertainties are indicated in both panels. The left plot shows binary fractions broken down by individual subclasses; upper (zero binaries) and lower limits (all binaries) are indicated by arrows. The right plot groups sources into spectral class bins of L0-L2, L2.5-L4.5, L5-L6.5, L7-L9.5, T0-T3.5, T4-T5.5 and T6-T8, with the number of source in each bin labeled. The overall observed binary fraction,  $\epsilon_b^{obs} = 20 \pm 4\%$ , is indicated by the dashed and dotted lines.